UNIVERSITY OF OKLAHOMA

GRADUATE COLLEGE

RESERVOIR CHARACTERIZATION AND CHEMOSTRATIGRAPHY OF THE GODDARD SHALE IN THE SOUTH CENTRAL OKLAHOMA OIL PROVINCE

A THESIS

SUBMITTED TO THE GRADUATE FACULTY

in partial fulfillment of the requirements for the

Degree of

MASTER OF SCIENCE

By

WILLIAM DAVIS RUSH
Norman, Oklahoma
2016

RESERVOIR CHARACTERIZATION AND CHEMOSTRATIGRAPHY OF THE GODDARD SHALE IN THE SOUTH CENTRAL OKLAHOMA OIL PROVINCE

A THESIS APPROVED FOR THE
CONOCOPHILLIPS SCHOOL OF GEOLOGY AND GEOPHYSICS

BY

_____
Dr. Roger M. Slatt, Chair

_____
Dr. Matthew J. Pranter

_____
Mr. Frederic Gallice

ACKNOWLEDGEMENTS

I would like to start by thanking Dr. Roger Slatt for his guidance throughout this project and my Master's degree as a whole. If not for him, none of this would have been possible and I would not be half the geologist I am today. I will never forget the day I showed up at his office for the first time and he offered me a position in the program, and I am eternally grateful for the experience I have gathered here and the opportunities it will present me. I would also like to thank Frederic Galllice for his support and willingness to work with us in providing data for the project as well as input on the interpretation. I would also like to thank Dr. Matthew Pranter for his input on the project and participation on my committee. I also wish to acknowledge Dr. Deepak Devegowda for his insight into geostatistics.

I owe a good deal of gratitude to Bryan Turner. His expertise in the use of handheld X-ray fluorescence analysis has been hugely influential in my work and growth as a geologist. His willingness to deal with my endless questions and provide support as well as his assistance in carrying out the scanning were invaluable.

I would also like to thank Jessica Tréanton not only for opening her home to Bryan and I during our work in Houston, but also for her incredible work on the chemostratigraphy of the Woodford which played a major role in this project.

Next, I would like to thank Gerhard Heij. His support in using the SEM and assistance in determining bedding planes on an apparently uniform sample were greatly appreciated.

I would like to thank the entirety of the Institute for Reservoir Characterization at the University of Oklahoma for the work produced by each of its members. Isaac Newton said “If I see further than others, it is because I stand on the shoulders of giants,” and if not for the work they have provided I would not have the inspiration or knowledge I needed to carry out this project. I would like to thank Jing Zhang, Daniela Becerra Rondon, and Henry Galvis Portilla in particular for their help in collecting data, as well as Carolina Mayorga for her work in porosity analysis and assistance in using Petra™.

I would be remiss if I did not also thank the incredible support staff of the ConocoPhillips School of Geology and Geophysics. Every member of our office has been incredibly supportive in issues ranging from fighting with the registration system to helping with the logistics of sample preparation and fieldwork to assisting in the acquisition of software for this project.

I would also like to extend my deep gratitude to Lance Ruffel. He took a chance on me by offering me the job that brought me out to Oklahoma and kickstarted my geologic career. I learned more about the business end of the oil and gas industry from him than any class could teach. He instilled in me that you cannot blindly accept what the instruments tell you with his constant refrain to “look at the rocks, not just the logs”.

Finally, I would like to thank all of my friends and family who supported me throughout this project. To all of my friends in Norman and Oklahoma City, especially Chas Wojan, Rachel and Thomas Neher, and Michael Roman, who kept me sane along the way with countless board game nights, road trips, and beer festivals, I would have cracked a long time ago without you guys. Thank you for listening to my rambling

about mudrock and X-rays. I also cannot thank my family enough, particularly Bob and Patti White who provided a familial welcome to a newcomer to the state and for helping me to establish myself here. Last but certainly not least, I would like to thank my mother whose unending support helped me see this through. What she has done for me means more to me than she could ever know.

TABLE OF CONTENTS

LIST OF TABLES

LIST OF FIGURES

ABSTRACT

The Goddard Shale of the South Central Oklahoma Oil Province, or SCOOP, has become a formation of interest in recent years. However, there is a paucity of published information in regards to this formation. Therefore, the purpose of this study is to provide a reservoir characterization of the formation by means of core description of lithofacies, chemostratigraphic trends, chemofacies, mineralogy, and porosity. Additionally, this study sets out to define the appropriate nomenclature for the formation, which has not been defined in a formal sense.

Descriptions and chemostratigraphic work were carried out on two cores taken from the formation. One was taken from its uppermost organic-rich bench, which this study refers to as the Boatwright Shale, and the other core was taken from the lowermost organic-rich bench, which this study refers to as the Velma Shale. Both cores are predominantly siliceous-argillaceous with carbonate content being restricted to debris flows from the inner shelf. Each core contains its own parasequence set with higher-order intervals superimposed, most easily defined by the changes in continental input by means of trace elemental proxies, although each has a different manifestation of the effects of rising sea levels.

In analyzing the porosity of the formation, this study compares three different techniques: 1) FESEM image analysis utilizing ion beam milling, 2) FESEM image analysis utilizing freshly broken shale surfaces, and 3) a method that relies upon calculated matrix density based upon Rock-Eval and XRD mineralogy. Of the three, the broken surfaces technique appears to have produced the most accurate results due to the

large margin of error in the calculated density technique and the general lack of inorganic porosity in the ion beam milling technique. Measured porosity values range from 7.04% to 13.11%.

1. INTRODUCTION

In the planning and development of any reservoir, a detailed reservoir characterization is an important step in maximizing the return on investment and exploiting the resource to its fullest potential. During times of falling oil prices, this is more important than ever, and the opportunity is provided to expand our understanding of existing reserves in order to cut down on wasted expenditures.

In recent years, the attention of the oil and gas industry has been drawn to the Goddard Shale formation of the Springer Group (Nash 2014). While the Springer Sands have been a rather prolific producing zone throughout the 20th century, to date, there has been a paucity of studies regarding the Goddard Shale. Located within the South Central Oklahoma Oil Province, or SCOOP, the Goddard Shale is an attractive target due to its potential for stacked pay zones with the well-developed late-Devonian Woodford Shale, the early-Chesterian Caney Shale, as well as the overlying Springer Sands. The purpose of this study is to provide a detailed characterization of two Goddard Shale cores, so that future development of this resource may be conducted more efficiently.

1.1 OBJECTIVES

Given the lack of published research on the Goddard Shale, this study seeks to answer some of the basic questions regarding the reservoir: 1) What is the lithology of the shale, i.e. is it siliceous, argillaceous, or carbonaceous? Touching on this further, what chemofacies are present within the formation? Is there any relationship between

trace elements and shifts in facies, particularly elements that may be detected by standard log tools such as uranium, thorium, and potassium? Going beyond this, what type of cyclicity is present within the system? Are the facies vertically homogenous, or is there an ordered cyclicity present? Based on the aforementioned qualities, it is possible to make inferences regarding changes in water depth, sediment input, and distance from shore during deposition. 2) What are the ranges of porosity values for the shale? While measuring porosity within unconventional reservoirs has provided a unique challenge for some time, there are a number of techniques that may be used to do so, and this study will analyze three: ion beam milling, SEM imaging of broken surfaces, and calculations based upon bulk density. 3) Finally, a simple but important question is, what should the formation as a whole and the units therein be referred to as? This formation has been referred to alternatively as both the Springer Shale and the Goddard Shale, which has led to a good deal of confusion within the existing literature. Due to the existence of a number of other shales within the Springer Formation, and to avoid further confusion, this study will refer to this shale as the Goddard Shale member of the Goddard Formation of the Springer Group. Even still, there is a further lack of consensus in the nomenclature of the individual units that make up the Goddard Shale. Two of these units, the uppermost and lowermost are described in this study. Therefore, this study posits that these units be referred to as the Boatwright for the uppermost unit, and the Velma for the lowermost unit.

1.2 GEOLOGICAL CONTEXT

Although the exact timing of the deposition of the Goddard Shale has been of some debate, the current consensus is that it appears to have been deposited during the late Chesterian stage at the boundary of the Mississippian and Pennsylvanian periods, roughly 325 million years ago (Westheimer 1956, Reedy 1968, Andrews 2001). The Goddard Shale is the uppermost unit of the Goddard formation, which serves as a basal unit of the Springer Group below the other unit, the Springer Formation, both of which are comprised of marine shales and scattered sandstone zones.

The Goddard Formation is comprised of the Goddard Shale, the Goodwin Sandstone, and the Goddard Sandstone, but the sands do not appear throughout the entire formation. Overall, the Goddard Formation mostly conformable to the underlying Caney Shale and Chester Limestone throughout the Anadarko Basin (Peace 1965, Andrews 2001). While the Caney Shale is typically black, brittle, and calcareous, the Goddard is dark gray, soft, clay-rich, and noncalcareous, and contains numerous bands of reddish-brown to orange-brown ironstone. The contact between the two may easily be determined via electric logs due to the low resistivity of the Goddard compared to the Caney (Westheimer 1956). (Figure 1)

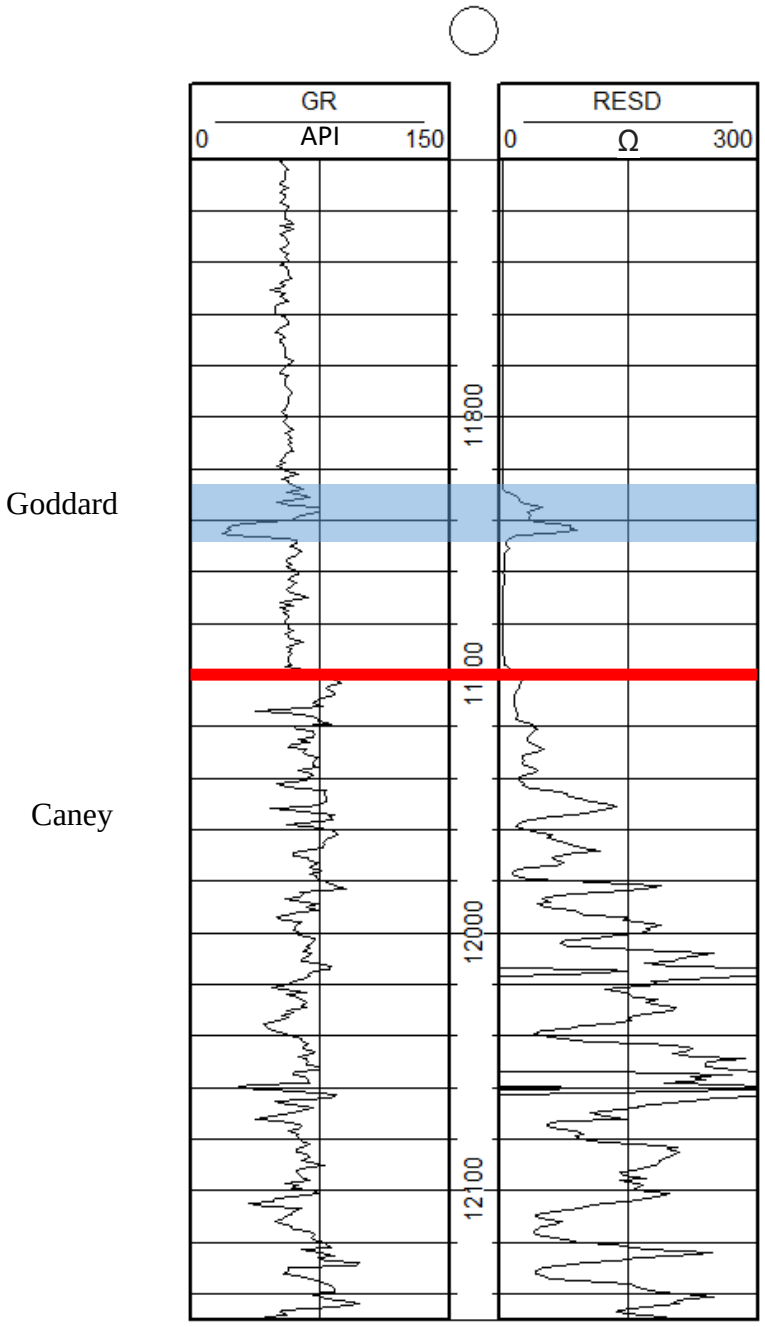

Figure 1. Contact between Caney Shale and Goddard Shale, indicated by change in resistivity and marked in red. The lowermost organic-rich bench, the Velma, begins at 11,854' and is highlighted in blue.

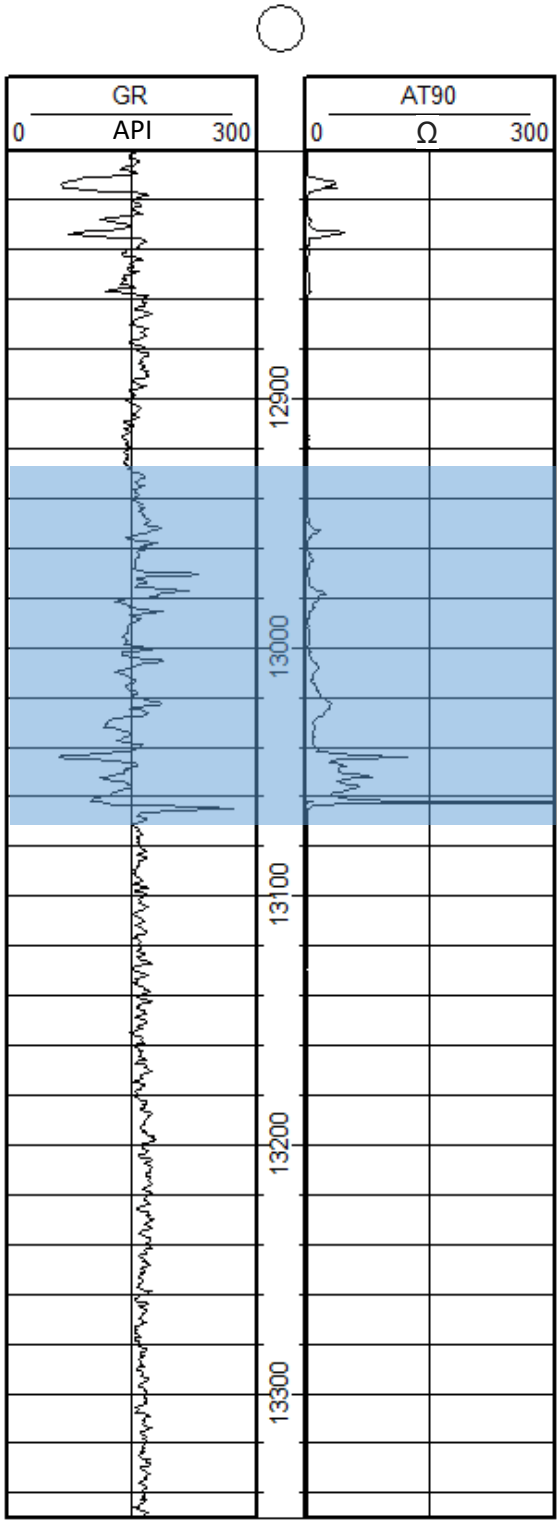

Figure 2. Well log covering the uppermost organic rich interval, the Boatwright, highlighted in blue.

The thickness of the Goddard Formation varies greatly, with a thickness of roughly 2850 feet at its type locality located on the Goddard Ranch at sections 18 and 19 of T3S-R4E, with the entirety of the Springer Group reaching a maximum of approximately 5000 feet near the Carter-Knox structure (Westheimer 1956, Peace 1965). Above, the Goddard is followed by a sequence of shales and sandstones, with the sandstones making up the majority of the Springer Group. The sandstone immediately overlying the Goddard Shale is known as the Boatwright Sandstone and is comprised of turbidite and off-shore bars (Andrews 2001). Many of the overlying sandstones have an established production history throughout much of the basin. These sandstones are typically bounded by an angular unconformity by the overlying Morrow Group. In some locations within the basin, the sands were deposited as incised valley deposits which eroded through older Springer Group strata into the Chester Limestone (Smith 1996, Andrews 2001).

The Goddard Shale contains three primary organic-rich zones. The uppermost organic-rich zone is removed by an unconformity in the north, but provides a potential target in its southern extent. The middle organic-rich zone, while too thin to be economical in the southern extent, is much thicker in the northern extent. The lowermost zone is somewhat thin in the southern extent, but may also be a target in the northern extent (Davis et al 2015). This study focuses on the uppermost bench, the Boatwright, and the lowermost bench, the Velma.

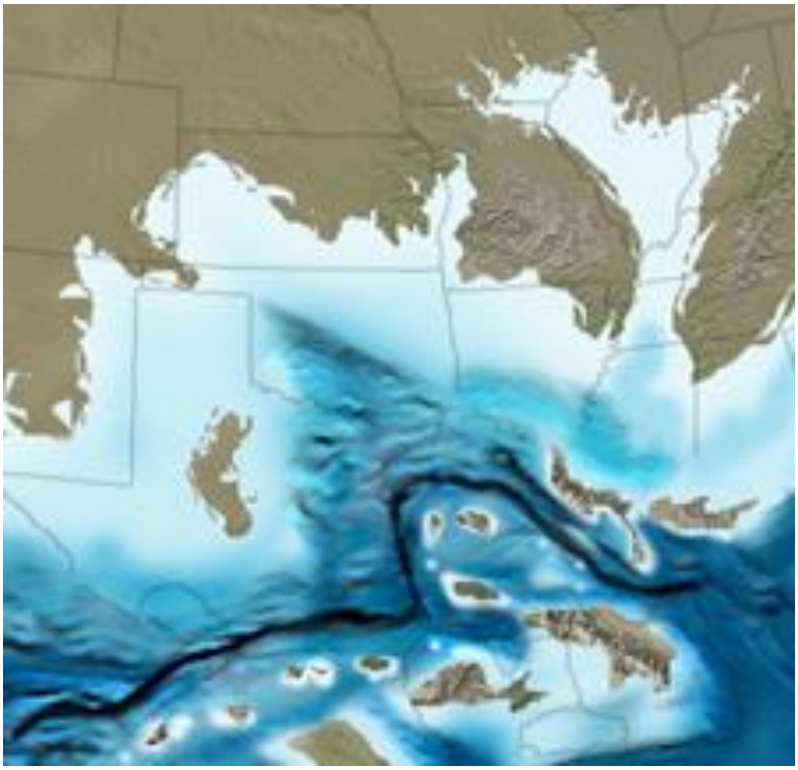

Figure 3. Paleogeographic map from the time during which the Goddard Formation was deposited. Deposition occurred primarily within the deeper portions of the epicontinental sea covering present day Oklahoma. Modified from Blakey 2013.

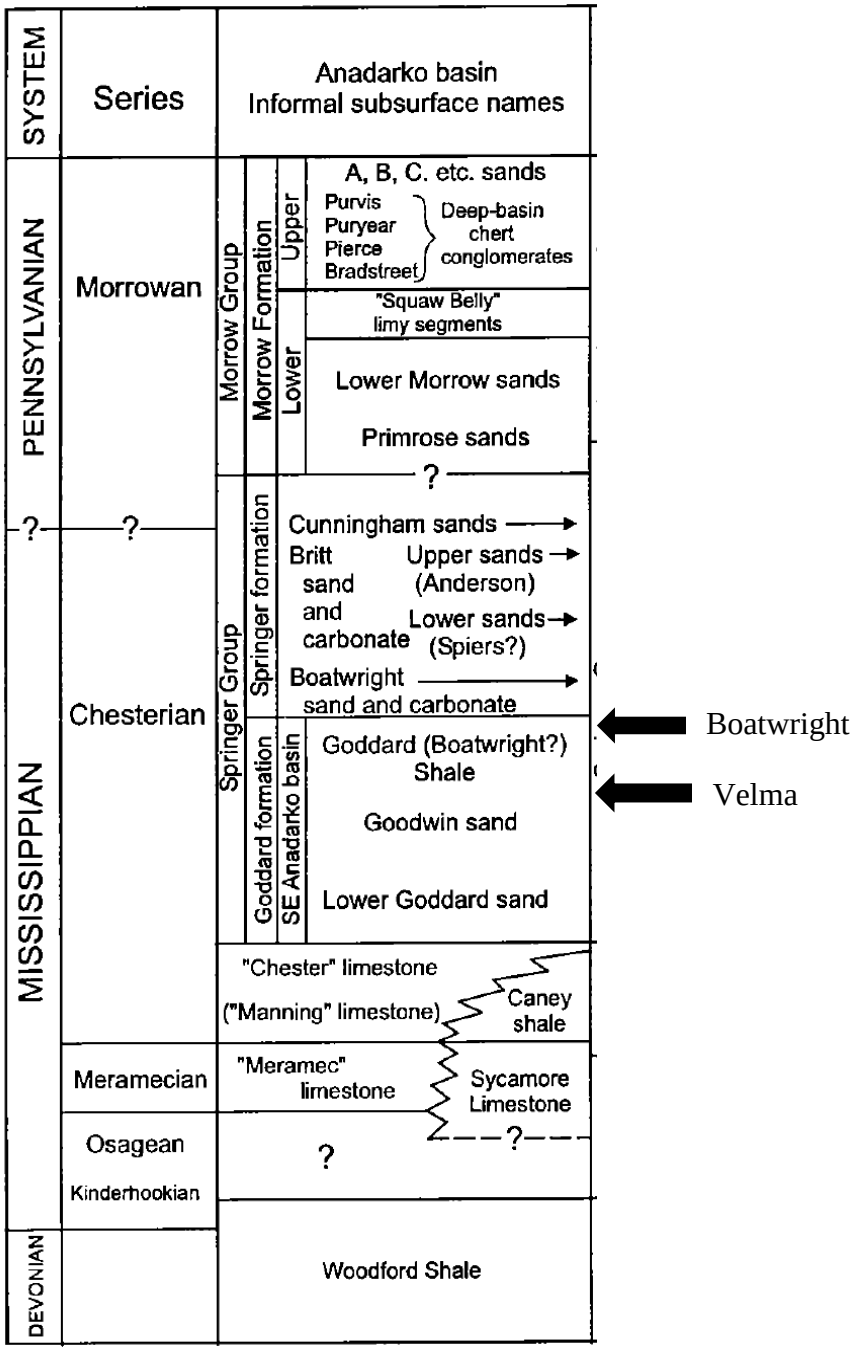

Figure 4. Stratigraphic Column of the Anadarko Basin. Note the position of the Goddard Formation within the Springer Group. Arrows mark the location of the two zones targeted, the upper Boatwright Shale, and the lower Velma Shale. Modified from Andrews 2001.

2. METHODS

Reservoir characterization draws upon a variety of datasets and analytical techniques. This study focuses on: (1) the identification of lithofacies based on core description; (2) the identification of chemofacies via XRF analysis of cores; (3) analysis of XRF data to determine characteristics of environment of deposition; (4) SEM imaging of fine scale features; (5) hardness testing via the use of a rebound hammer; and (6) porosity analysis and a comparison of values derived from ion beam milling, SEM imaging of freshly broken surfaces, and calculations of bulk matrix density.

2.1 DATA AVAILABLE

The primary sources of data for this study were taken from cores. The first core, which measures 145 feet and 10 inches, was taken from section 17 of T4N-R5W within Grady County, Oklahoma, and is comprised of the uppermost organic-rich facies of the Goddard formation. Five samples were taken from this core for X-ray diffraction analysis and to produce thin sections. The second core, which measures 33 feet and 11 inches, was taken from section 33 of T1N-R5W within Stephens County, and is comprised of the lowermost organic-rich facies of the Goddard formation. X-ray diffraction data, from both bulk and oriented samples, from 32 samples and ion beam milling derived porosity values from 5 samples were provided from the first core by the well's operator. Thin section photographs were also provided for 31 of the intervals analyzed by XRD. Five sidewall cores taken from the first well were made available and used for porosity analysis. Gamma ray scans of each core were provided by the wells' operators.

Two cores, one of the Boatwright and one of the Velma, were described at a one inch resolution. Elemental composition was obtained of the cores at a 2 inch resolution. Rebound hammer measurements were taken of the Velma core at a 2 inch resolution, with 5 readings being taken at each interval in order to obtain an average value. X-ray diffraction data (XRD) was provided for each of the cores. Thin sections and rough samples were analyzed under SEM, including both scanning electron and backscatter analysis on samples taken from the Boatwright core. Sidewall cores were provided of the Boatwright core from 5 intervals outside of the primary cored interval, and were analyzed via X-ray diffraction and Rock-eval. Volume and mass of these samples were also measured.

Figure 5. Map showing location of cores. Boatwright was taken from the northern location in Grady County and the Velma from the southern location in Stephens County.

2.2 ANALYTICAL METHODS

2.2.1 Inorganic Geochemistry

X-ray fluorescence analysis (XRF) was performed on both cores using a Bruker Tracer IV-SD handheld XRF™ at a 2 inch resolution for both trace and major elements. The XRF scans were calibrated at 40 kEV accelerating voltage, 30μA current, with a 1mil Ti- 12mil Al filter and vacuum applied for the trace elements. For the major elements, the XRF was calibrated at 15 kEV accelerating voltage, 10μA current, with no filter and without the use of the vacuum. A scanning time of 30 seconds was used at each interval. Relative proportions of elements, reported in ppm, were compared against each other to establish correlative relationships. Statistical analysis of this data by means of hierarchical clustering analysis was performed using the Minitab 17™ statistics package developed by Minitab, Inc. In the hierarchical clustering analysis, Ward linkage and Euclidean distances were used in determining similarity. In determining the number of clusters, similarity level was considered, but not used as the primary determinant in where to divide one cluster from another. Instead, an iterative process was used in which a predefined number of clusters were calculated; the average abundance of each element within each cluster was calculated and divided by the average abundance of each element within the core as a whole in order to provide a ratio demonstrating the increased concentrations in some facies and the decreased concentrations in others. The process was repeated with various numbers of clusters until geologically realistic results were obtained, taking into account the level of

similarity within clusters. Elements used in the determination of clusters included: titanium (Ti), zircon (Zr), potassium (K), aluminum (Al), molybdenum (Mo), vanadium (V), calcium (Ca), strontium (Sr), phosphorus (P), magnesium (Mg), silicon (Si), silicon/aluminum ratios, and silicon/titanium ratios.

Table 1: Elements as proxies for minerals provided a means to predict paleoenvironment

Element	**Paleoenvironmental Interpretation**	**Limitations**
Ti *[1]	Terrestrial clastic provenance	Can be transported via aeolian processes
Zr *[1]	Terrestrial clastic provenance	Can be transported via aeolian processes
Si *[1]	Detrital or biogenic provenance	Dual origin possible
Al *[1]	Contained in clays and potassium feldspar	Terrestrial fluvial
K *[1]	Contained in clays and potassium feldspar	Terrestrial fluvial
Mg *[2]	Contained in carbonates (Dolomite and Magnesite)	Marine and diagenetic origin
Ca *[2]	Contained in carbonates	Marine and diagenetic origin
Sr *[2]	Contained in carbonates	Marine and diagenetic origin
Mo *[3]	Sequestered mainly in anoxic conditions	Basin restriction *[4] Can be concentrated in phosphates
U *[3]	Sequestered mainly in anoxic conditions	Basin restriction *[4]
V *[3]	Sequestered mainly in anoxic conditions	Basin restriction *[4]

Cr *[3]	Sequestered mainly in anoxic conditions	Basin restriction *[4]
Co *[3]	Sequestered mainly in anoxic conditions	Basin restriction *[4]
P *[5]	Sequestered under oxic conditions Bionutrient: may be indicative of increased productivity	Solubilized under anoxic conditions *[2]
Cu *[3]	Delivered in association with organic material	Typically requires presence of iron and sulfur to become incorporated
Ni *[3]	Delivered in association with organic material	Typically requires presence of iron and sulfur to become incorporated
Zn *[3]	Delivered in association with organic material	Typically requires presence of iron and sulfur to become incorporated
Modified from Treanton (2014) *[1] Sageman and Lyons (2004) *[2] Brumsack (2006) *[3] Tribovillard et al. (2006) *[4] Algeo and Rowe (2012) *[5]Harris et al. (2013)		

2.2.2 Core Description

A detailed description of the core was performed at one inch resolution based on a modified version of the description guidelines outlined by Lazar et al (2015) and the core description/visualization method outlined by "Ozzy's core log". Noted features included: fissility of the shale, continuity, parallelism, and orientation of laminae, bioturbation, apparent changes in mineralogical composition, presence of fossils, presence of nodules, and presence of natural fractures and slickensides. Five thin sections were taken from the core for finer detailed analysis of sedimentary features via SEM imaging.

2.2.3 Porosity Analysis (SEM)

In calculating the porosity of the shale, a variety of methods were used and checked against each other in order to find the most accurate values possible. Porosity values derived from ion beam milling and field emission scanning electron microscopy (FESEM) were provided by the company that extracted the core. However, the accuracy of the ion beam milling technique has been called into question regarding the destruction of intergranular porosity during the milling process (Slatt et al. 2013). An alternate scanning electron microscopy technique is outlined by Slatt et al. (2013). This technique relies upon a series of 10 images taken at a 4000x zoom on freshly broken surfaces created on three mutually perpendicular sides of a cubic sample. The contrast and brightness of these samples are altered to highlight porosity. Jmicrovision™ software was then used to determine the percentage of each image comprised of pore space as well as providing information on the size and distribution of sizes of the pores. The broken surfaces technique is limited in that plucked grains can provide indentations that can be mistaken for pores. Both techniques are limited in that depending upon the brightness and contrast values used, there may be some degree of variation in the results.

2.2.4 Porosity Analysis (Calculated Density)

Given the issues inherent in the previous techniques, a third measurement of porosity was tested. Total porosity may be calculated using the formula Porosity (weight %) = 1-(Bulk Density/Grain Density) in which grain density is the weighted average of the density of the component minerals and kerogen content. X-ray diffraction analysis was used to determine the mineralogy of 5 samples taken from

sidewall cores from the Boatwright shale. Rock-eval was conducted on 5 adjacent samples to determine total organic content. The known densities of the mineralogy were used to calculate the grain density, with minerals of varying densities, namely clay minerals, using an averaged density of their ranges. Kerogen has a density of 1.0 g/cm^3 to 1.4 g/cm^3 depending on the maturity of the sample. Samples were determined to be moderately mature based on the Rock-eval analysis (calculated Ro=1.07-1.12), therefore a value of 1.2 was used. Volume of samples taken adjacent to the samples used for rock-eval and X-ray diffraction was calculated using water displacement in a 10 mL graduated cylinder. The samples were then crushed and heated in a degassing chamber to drive off any volatile compounds which may contribute to the density, i.e. fluid density derived from formation water and hydrocarbons. The mass of the samples was measured after degassing and used to calculate the bulk density. This technique again has its own inherent problems in the varying densities of some of the minerals as well as the error that may be introduced in the volume and mass measurement techniques. However, it is the hope of this study that by using a variety of measurement techniques, some degree of reproducibility and accuracy may be achieved.

3. RESULTS

3.1 CORE DESCRIPTION

Overall, the Goddard Shale described within both cores is a siliceous-argillaceous mudrock with limited carbonate content (0-8.9%); the exception to this rule is isolated dolomite beds which are present within each core. Both cores overall demonstrate a high order fluctuation among units dominated by quartz and units dominated by clay minerals. The core taken from the Velma exhibited a much higher frequency of cyclicity, with both a greater number of facies as well as a more rapid transition between them. In both cores, the clay rich facies took on a "poker chip" appearance. The Velma core also exhibited a greater number of natural fractures than the Boatwright core, likely due to it being taken from a more structurally deformed area.

Table 2: Lithofacies within the Boatwright Core

fPN	Highly fissile black mudrock with interspersed pyrite grains ranging from very fine to up to ¾ in in diameter in rare cases. Contains numerous nodules and pyritized burrows throughout.
LP	Black mudrock with defined, continuous, parallel, planar laminations containing fine-grained pyrite. Typically lacks nodules.
BM	Black, massive mudrock. No apparent laminae or nodules
fLP	Similar in appearance to LP, but with a moderate degree of fissility. Nodules more common.

MC	Black murock containing mud clasts. May contain pyrite.
LM	Black mudrock with laminations ranging 1-10 mm thick, typically continuous, parallel, planar, but sometimes wavy and nonparallel with a varying degree of continuity. Laminations typically are grey-light-grey, but sometimes are brown.
fLM	Similar in appearance to LM, but with a moderate degree of fissility. Nodules are more common.
CPB	Convoluted pyritized beds. Typically concurrent with nodules of apatite. Apparent reworking of sediment. SEM analysis revealed the presence of biogenic material such as sponge spicules and radiolarians. These were largely absent in other thin sections.
fBM	Similar in appearance to BM, but with a moderate degree of fissility.
GM	Light colored, massive mudrock. Contains large amounts of dolomite.
CB	Convoluted bedding. Apparent reworking of sediment with mix of light and brown minerals.
fCB	Similar in appearance to CB, but with a moderate degree of fissility
PM	Massive pyrite-rich facies.
N	Core dominated by nodule. Contained only natural fractures within the core.

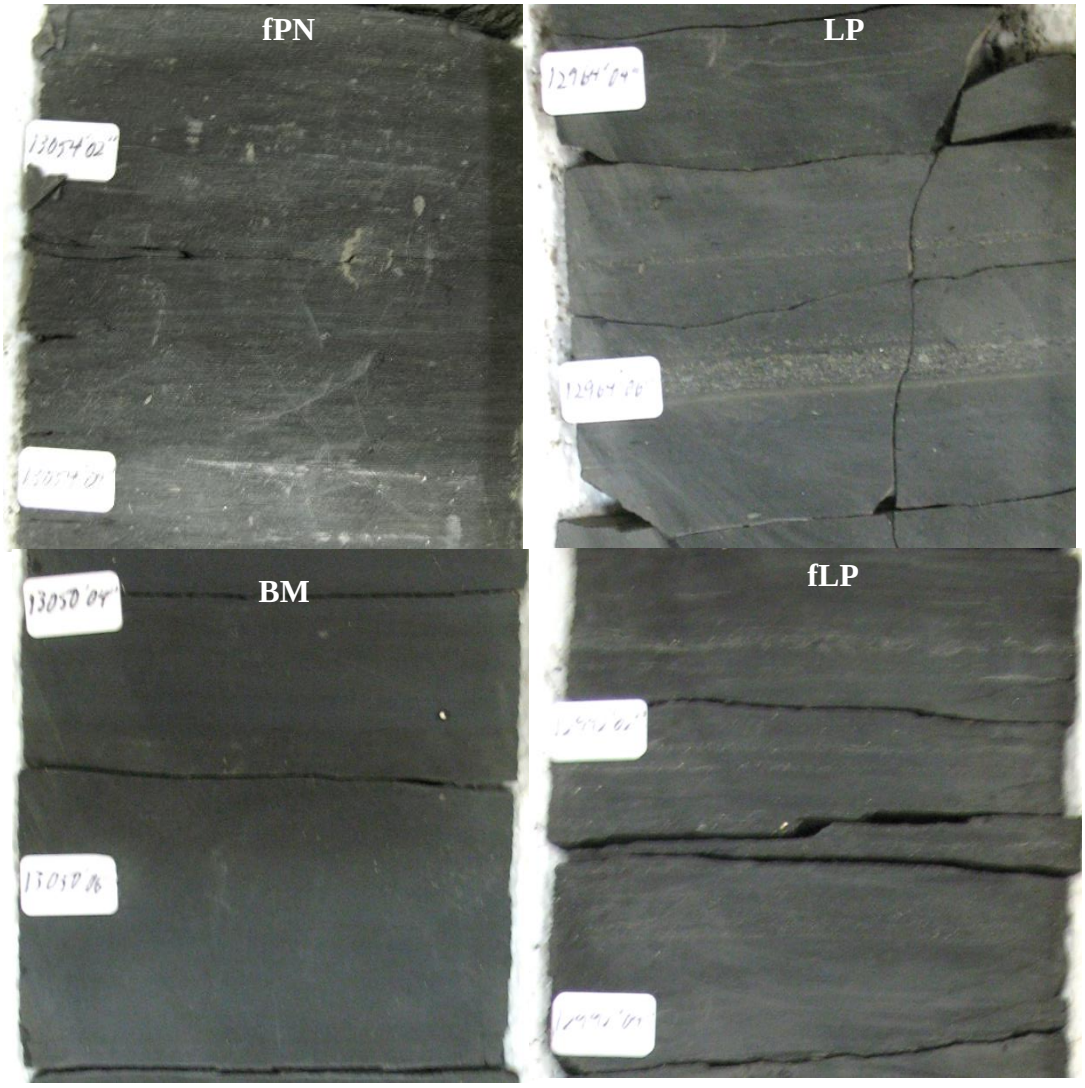

Figure 6. Examples of lithofacies within Boatwright core. From left to right, then top to bottom: fPN, LP, BM, fLP.

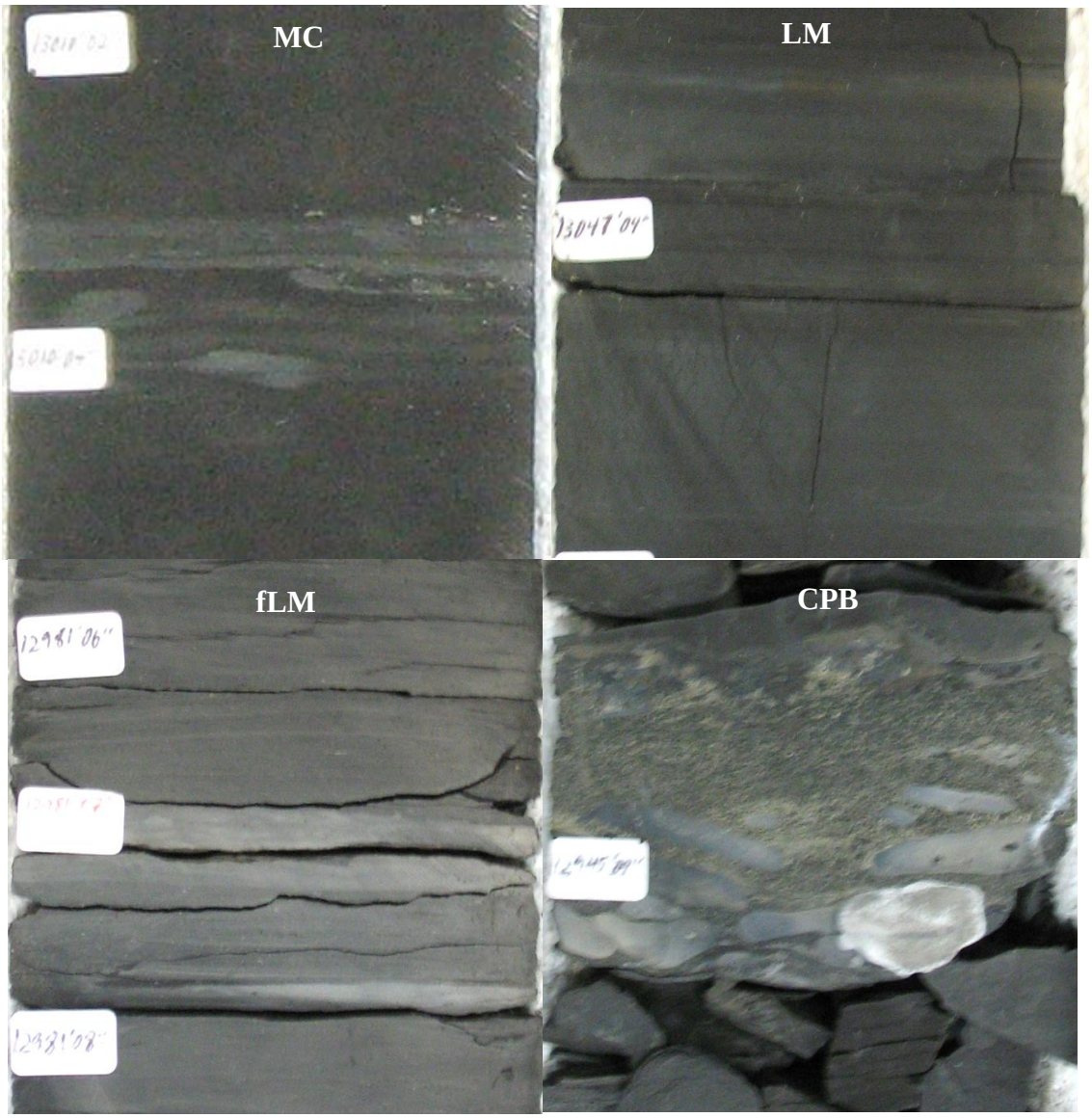

Figure 7. Examples of lithofacies within Boatwright core. From left to right, then top to bottom: MC, LM, fLM, CPB.

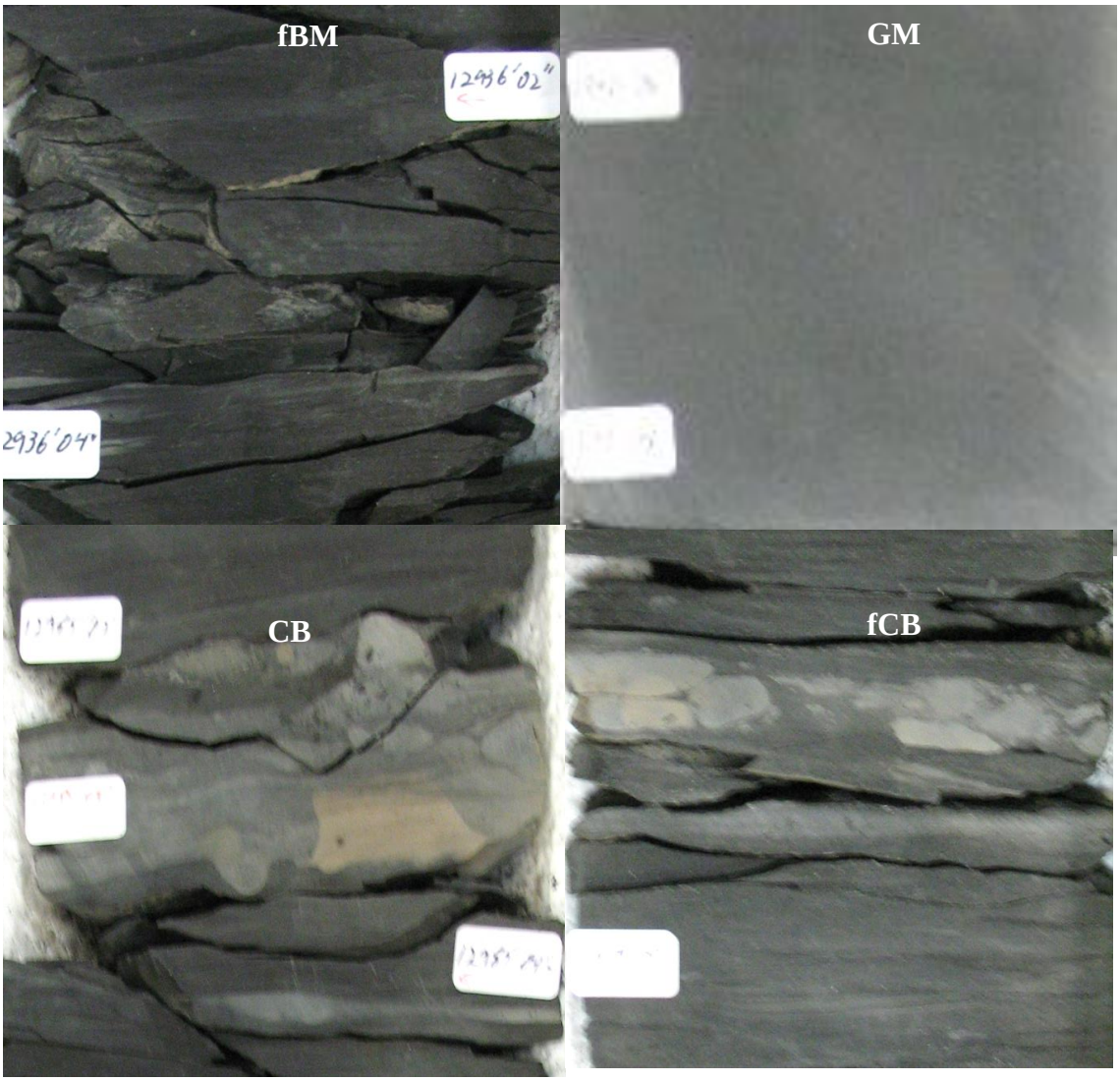

Figure 8. Examples of lithofacies within Boatwright core. From left to right, then top to bottom: fBM, GM, CB, fCB.

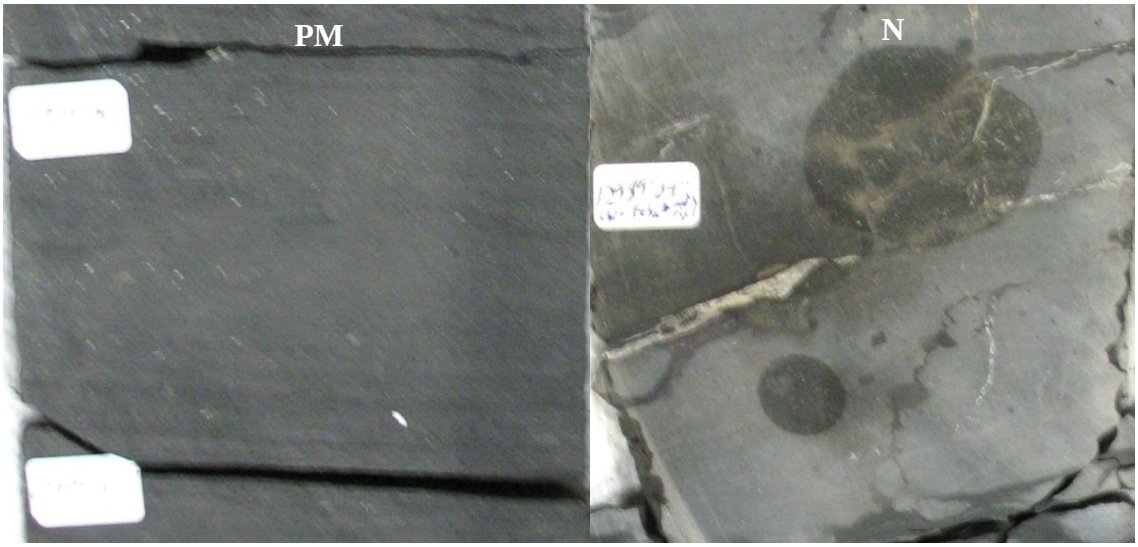

Figure 9. Examples of lithofacies within Boatwright core. From left to right: PM, N.

The base of the Boatwright core is dominated by the fissile, pyritized, nodule-rich facies (fPN) from 13081’ to 13052’09”. Throughout this section, there is a relatively high degree of bioturbation that is largely absent throughout the rest of the core. This facies rapidly transitions into much more siliceous facies (Figures 6 & 7: BM/LM) with convoluted, pyritized beds (Figure 7: CPB) at the transition. (Figure 10) Analysis of a thin section taken from this pyritized bed revealed a number of microfossils, including radiolarians and sponge spicules, which appear to be largely absent in thin sections taken from other facies. (Figures 11-13)

From 13033’ to 13030’07”, the core is highly dolomitized (Figure 15, Figure 8: GM). This transition is sharp at the base, but there are alternating laminations between the dolomite-rich facies and the siliceous facies as it transitions back into the siliceous facies. The dolomite facies overall is rather massive, but there are discrete pockets of quartz sand within it.

Moving up through the core, the quartz content gradually decreases as the clay content increases. At 12993’, the core transitions more completely back into a more fissile facies (Figures 7 & 8: fBM/fLM), although not to the degree of the basal unit. This transition again contains convoluted, pyritized beds (Figure 7: CPB). At 12972’05”, the mudrock becomes much less fissile, increasing in silica content (Figures 6 & 7: BM/LM). At 12963’, the core becomes fissile again, and this cyclicity between fissile and siliceous facies continues onwards throughout the remainder of the core in short intervals. (Figure 16)

Natural fractures are largely absent throughout the Boatwright core. The only instances in which natural fractures were recorded were within nodules (N), all of which

were recemented. In addition to the high degree of pyrite present within the lower unit and the very high concentrations within the pyrite beds, there are very fine pyrite grains scattered throughout much of the core. A detailed core description at a one inch resolution with facies codes and data visualization can be found in appendix A.

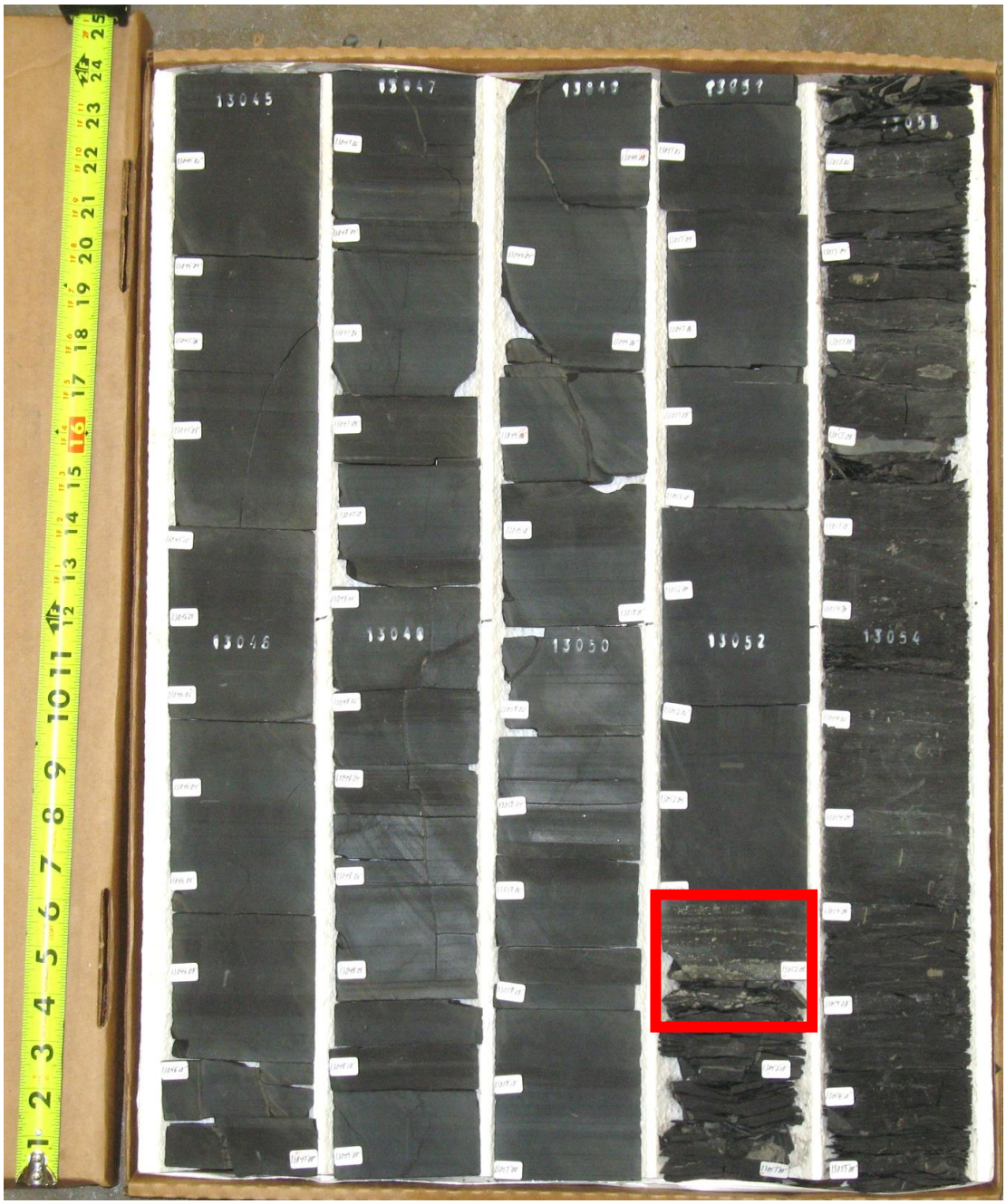

Figure 10. Transition zone between fissile, clay-rich facies at base of core of upper unit and more siliceous interval at 13,052'07". Note pyritized zone at transition between facies, outlined in red.

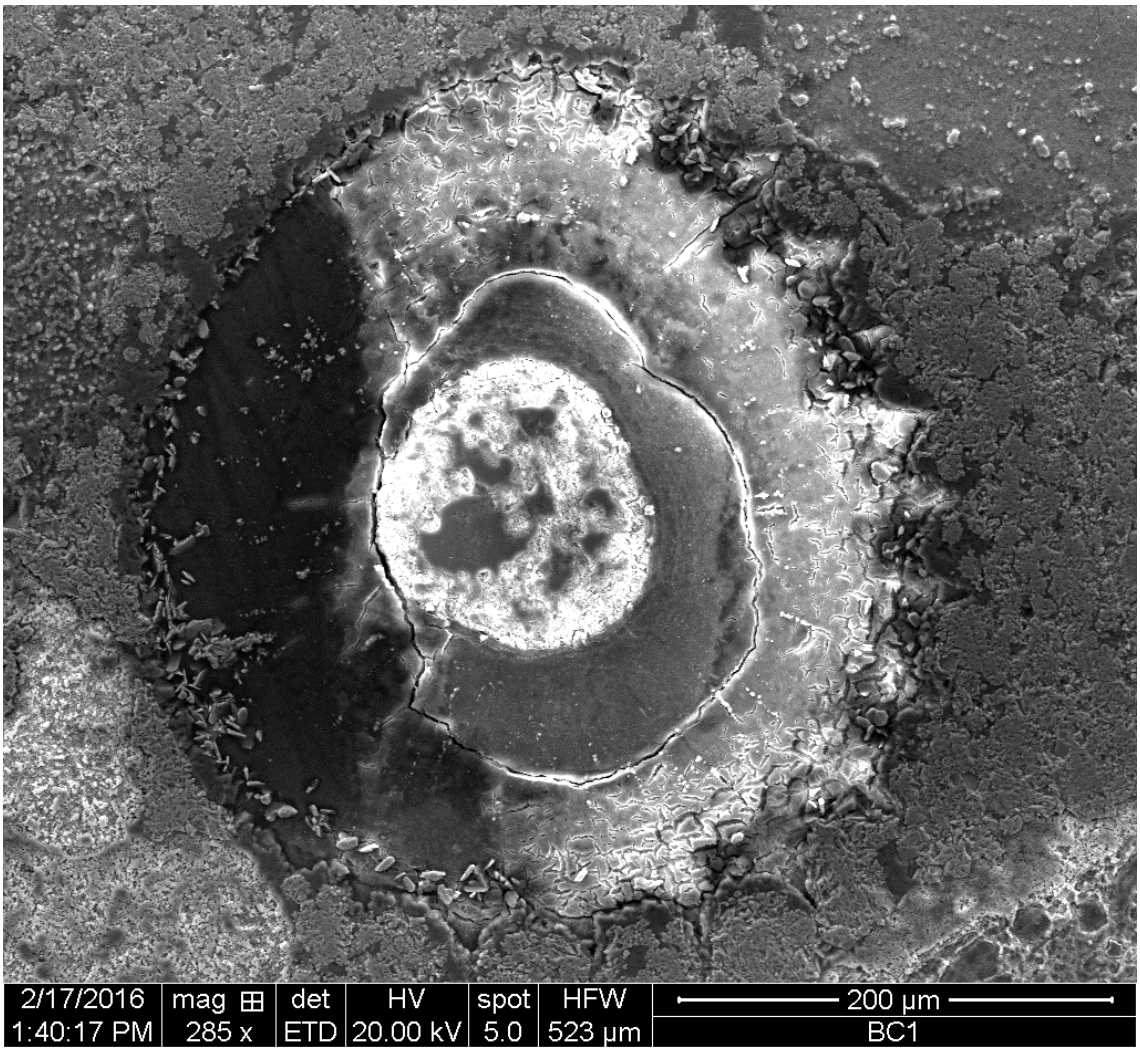

Figure 11. Scanning electron microscopy image of radiolarian taken from pyritized zone at transition between facies in figure 9. Fossils were notably absent in other thin sections.

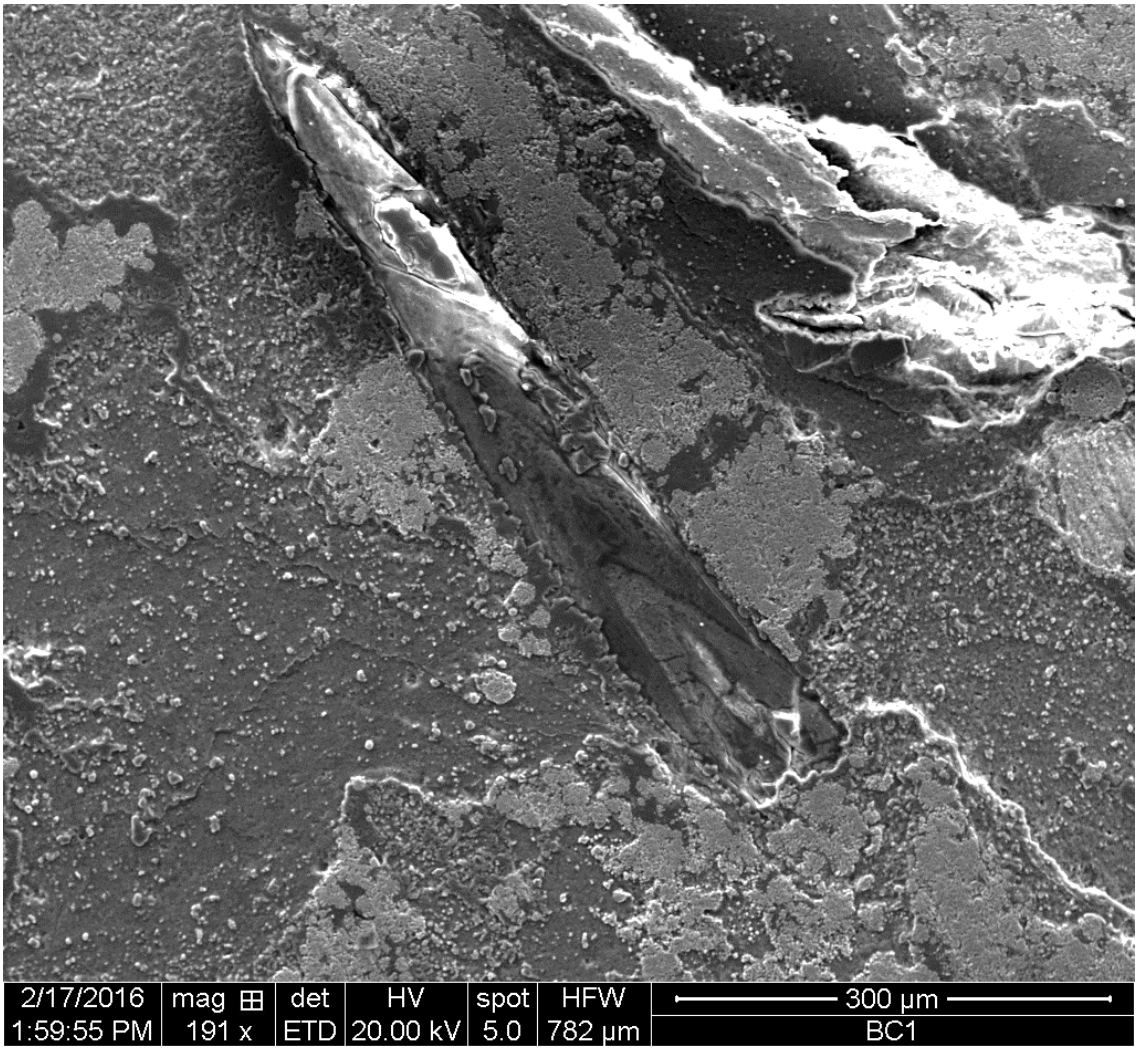

Figure 12. Megascleres sponge spicule found in pyritized zone at transition between facies in figure 9.

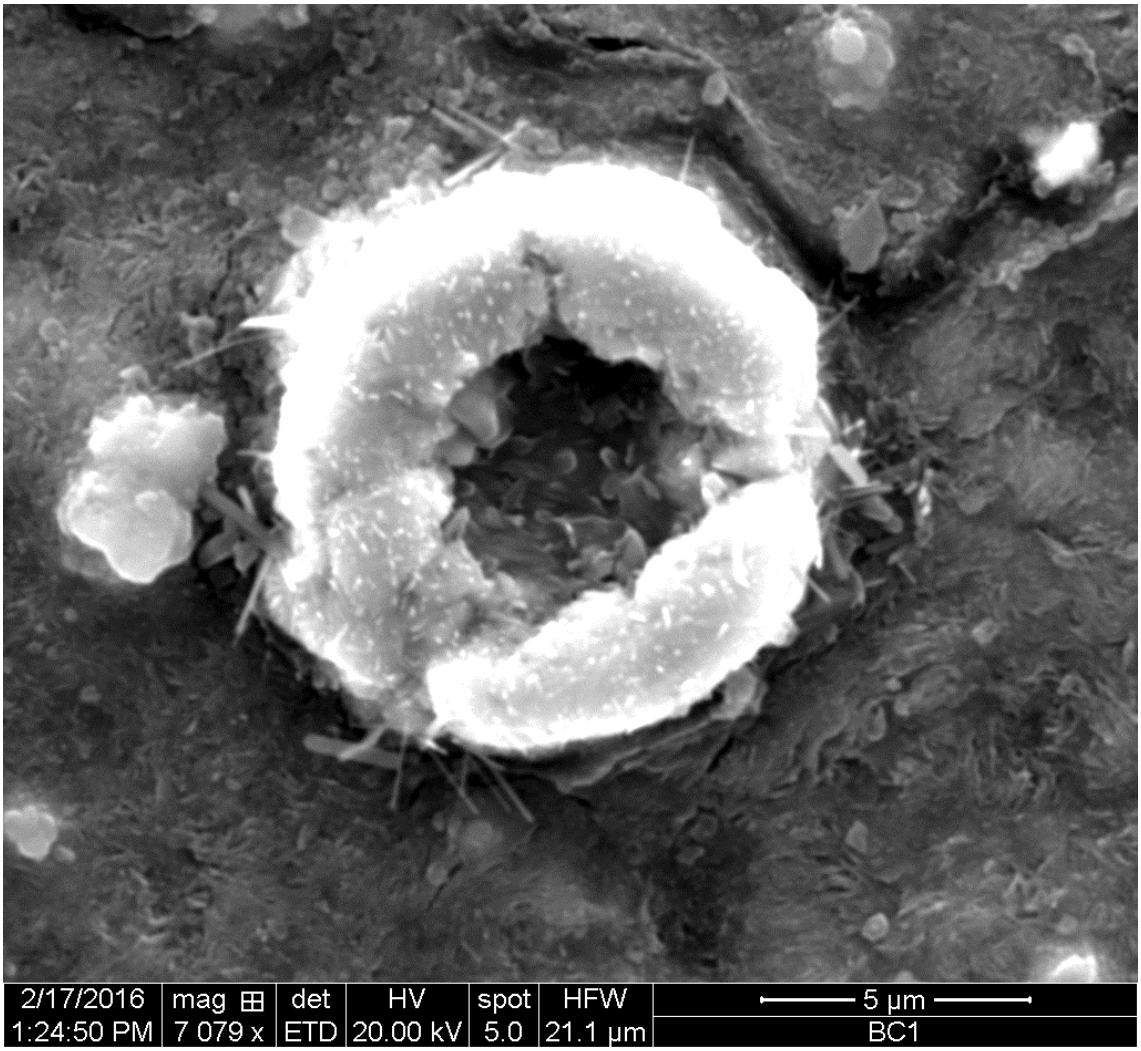

Figure 13. Microscleres sponge spicule found in pyritized zone at transition between facies in figure 9.

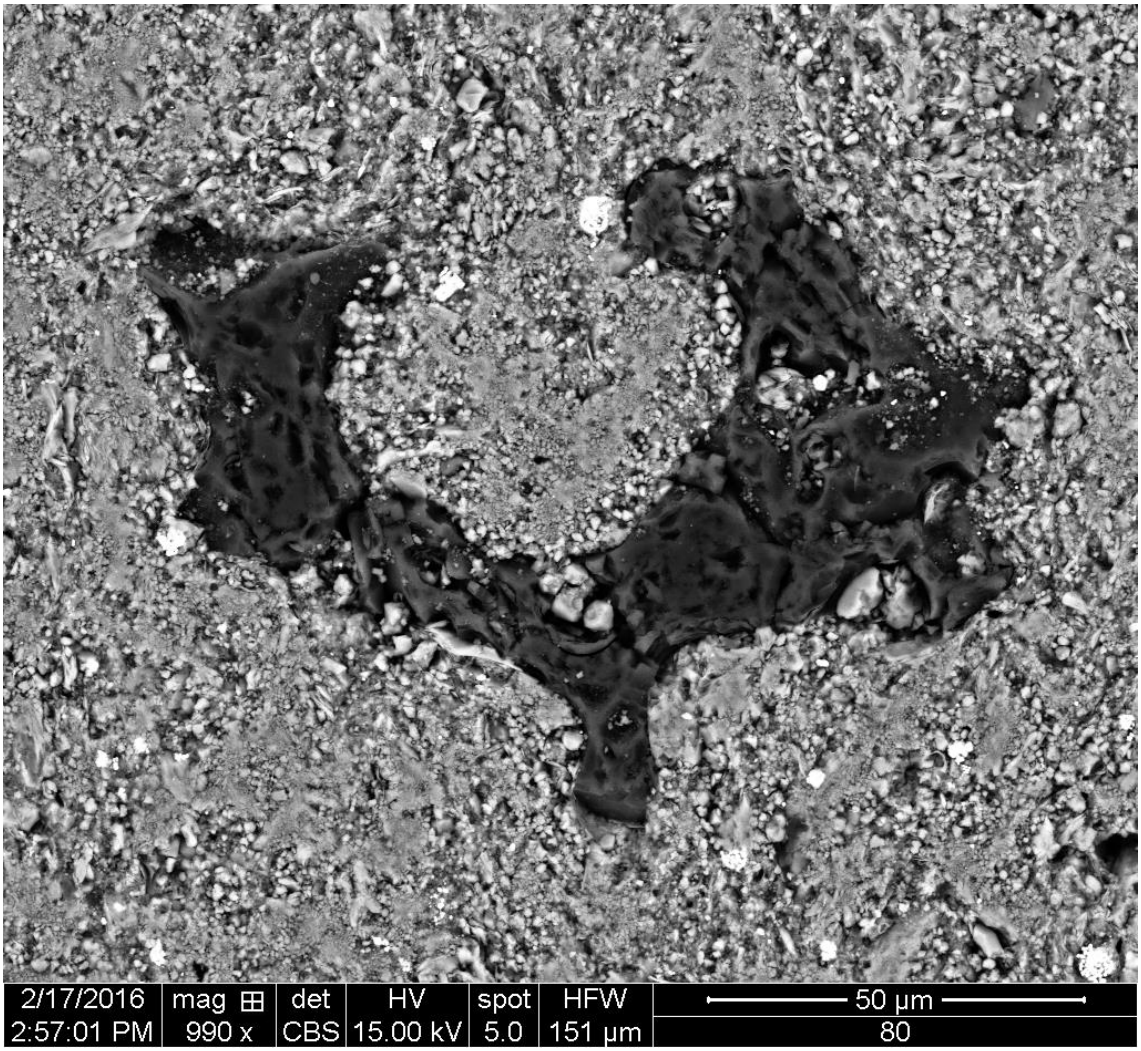

Figure 14. Backscatter image of kerogen found in core.

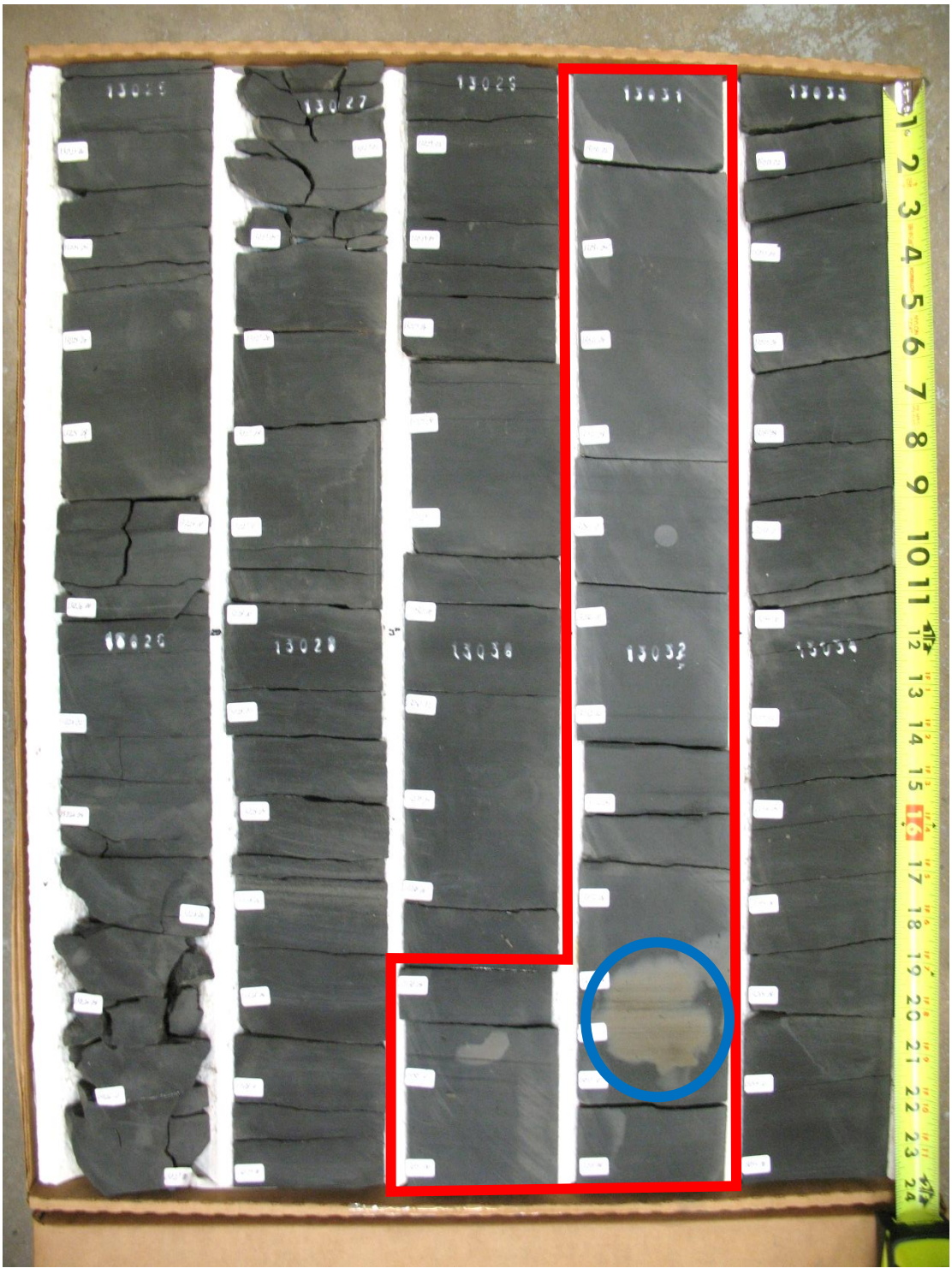

Figure 15. Section of Boatwright core containing dolomitized interval beginning at 13,033' and transitioning out beginning at 13,030'10", outlined in red. Note the pocket of quartz sand at 13,032'09", outlined in blue.

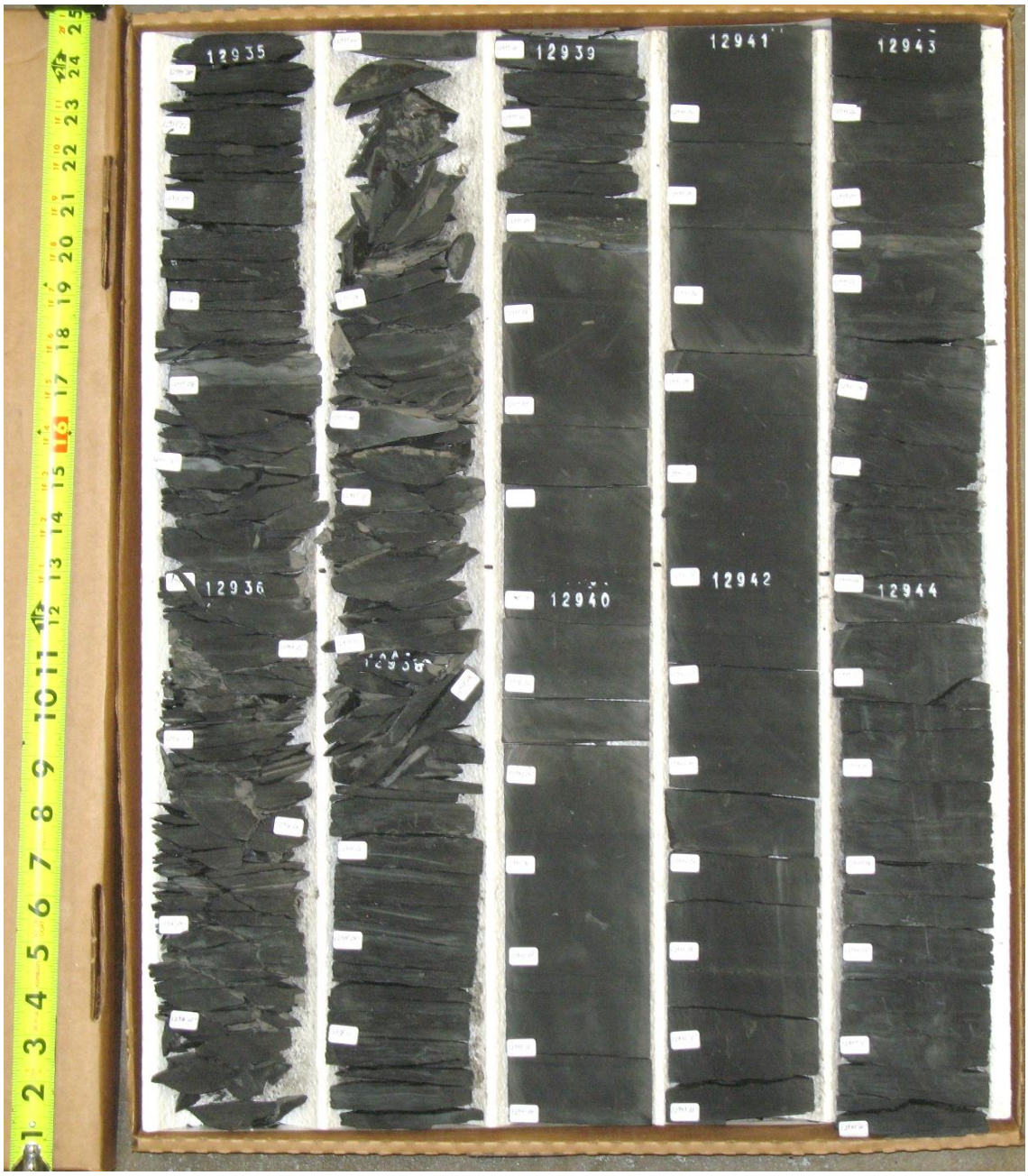

Figure 16. Uppermost extent of Boatwright core displaying higher ordered cycle. Note moderate fissility between 12,945' and 12,943' which becomes more consolidated between 12,943' and 12,939'04" before becoming highly fissile in the remainder of the core. Fissile facies are associated with high clay content and high terrigenous input.

Table 3: Lithofacies within Velma Core

BBF	Fissile mudrock with black and brown laminations
BlL	Black mudrock with white laminae, typically wavy, nonparallel, with varying degrees of continuity wherein the majority are under 1 cm thick, may contain occasional thick lamination.
BlT	Black mudrock with laminations over 1 cm thick. Typically continuous, planar, and parallel
BrT	Brown mudrock with laminations over 1 cm thick. Typically continuous, planar, and parallel
BrM	Brown massive mudrock, no apparent laminations
BlM	Black massive mudrock, no apparent laminations
CS	Coarse sand
N	Core dominated by nodule
CL	Laminations comprised of coarse sediment
DDFMD	Dolomite debris flow, massive, dark in color
DDFML	Dolomite debris flow, massive, light in color
DDFCD	Dolomite debris flow, poorly sorted coarse material, dark in color
DDFCL	Dolomite debris flow, poorly sorted coarse material, light in color
BrL	Brown mudrock with laminations
BrF	Massive brown mudrock, fissile
BlF	Massive black mudrock, fissile
BlSL	Black mudrock with grey, sandy laminations. Less coarse than CL.

BBFD	Mudrock with black-brown laminations, fissile, and dark in color
BBL	Similar to BBF, but lighter in color

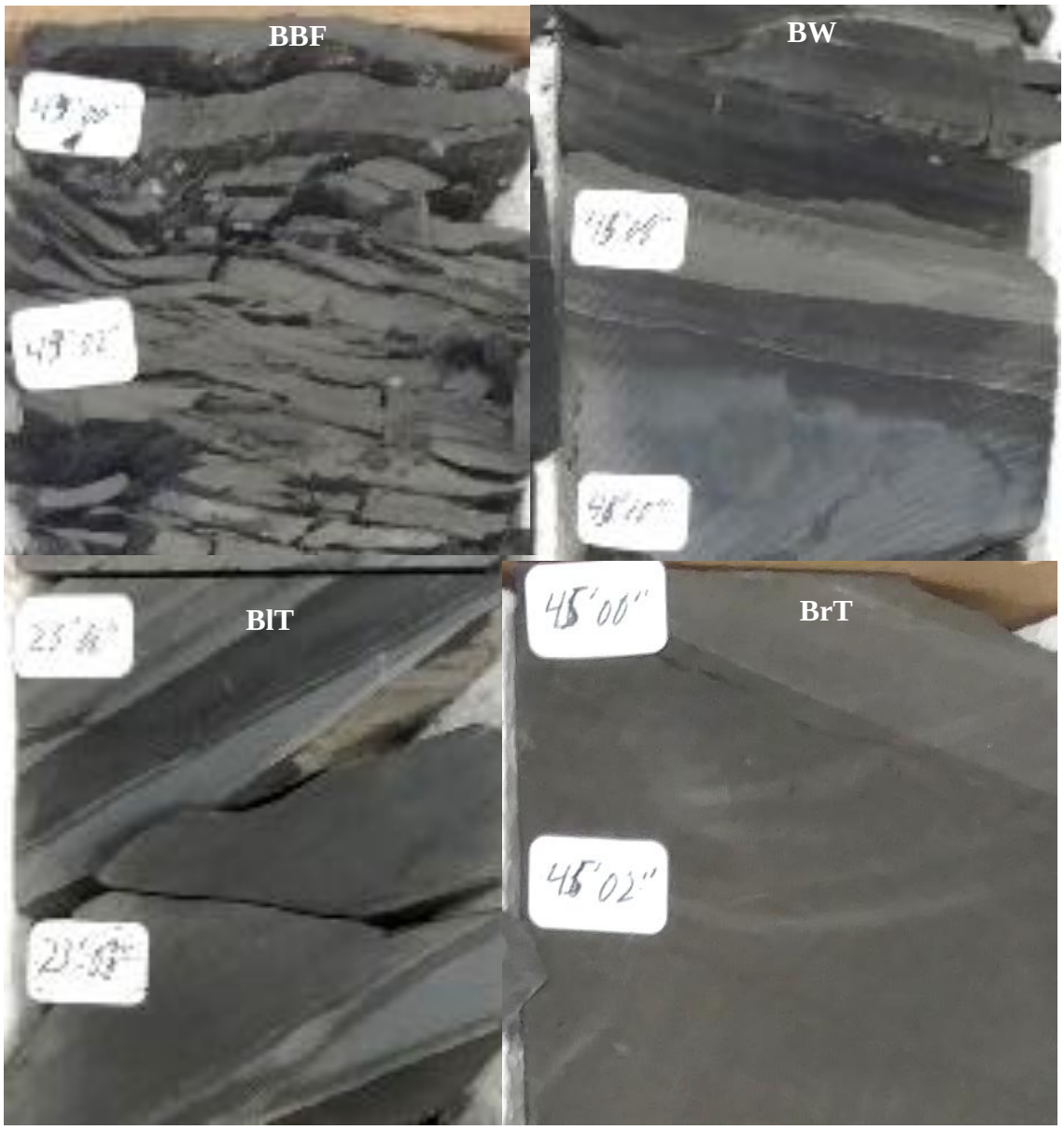

Figure 17. Examples of lithofacies within Velma core. From left to right, then top to bottom: BBF, BW, BlT, BrT.

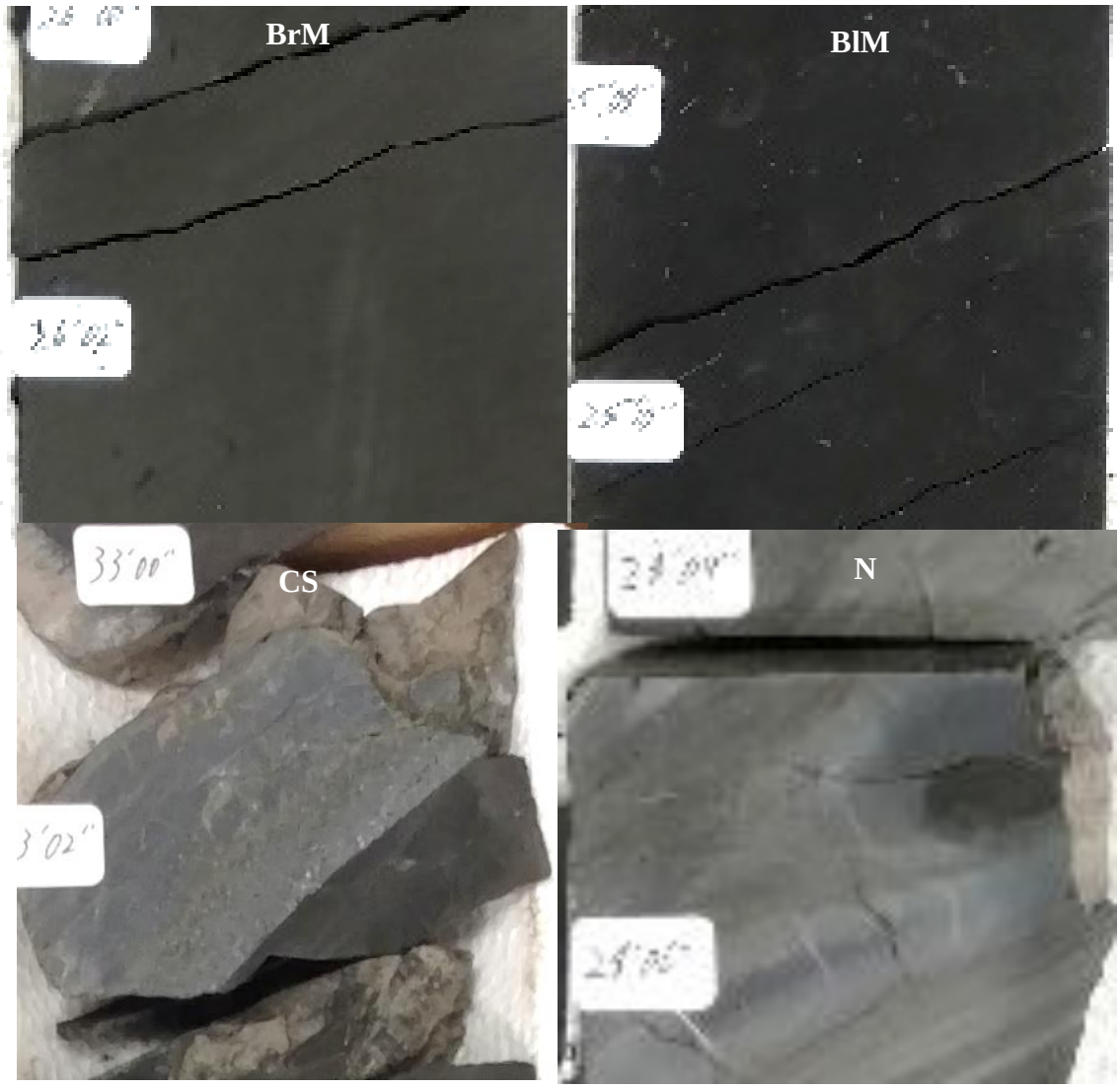

Figure 18. Examples of lithofacies within Velma core. From left to right, then top to bottom: BrM, BlM, CS, N.

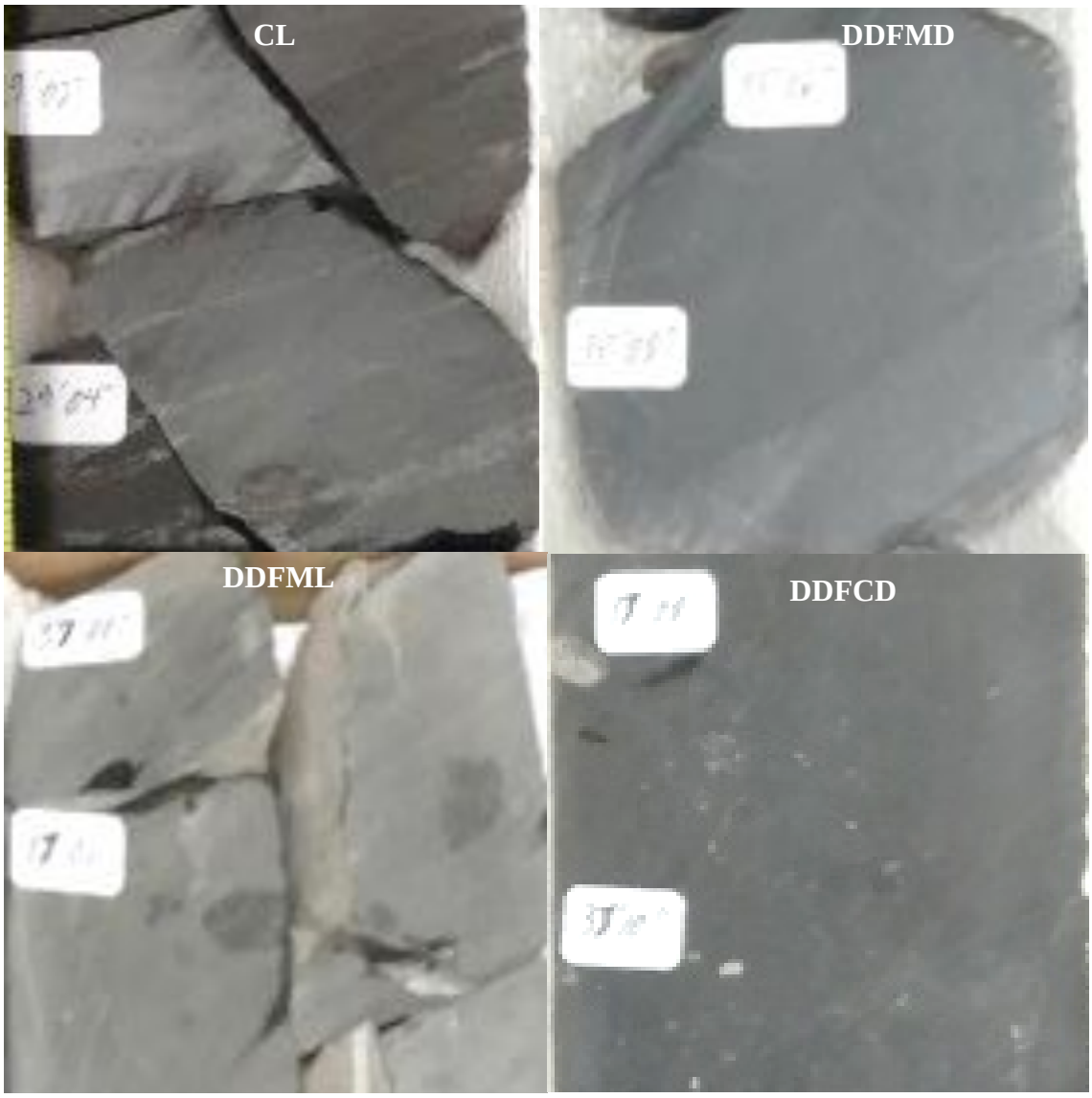

Figure 19. Examples of lithofacies within Velma core. From left to right, then top to bottom: CL, DDFMD, DDFML, DDFCD.

Figure 20. Examples of lithofacies within Velma core. From left to right, then top to bottom: DDFCL, BrL, BrF, BlF.

Figure 21. Examples of lithofacies within Velma core. From left to right, then top to bottom: BlSL, BBFD, BBL.

Despite covering a smaller interval (35 feet), the Velma core exhibits a greater amount of variance than the Boatwright core, with facies changes occurring much more frequently. The base of the Velma core also begins with a rather clay-rich facies at 11,854’ to 11,845’10”. This section is marked by black and brown continuous, wavy-planar, nonparallel laminae in varying ratios, i.e. some sections have an increased amount of brown laminae compared to black (Figure 22, Figures 17 & 21: BBF/BBFD).

The core is generally more consolidated from 11,845’10” to 11,843’06”. Within this consolidated unit are discrete intervals of black and brown mudrock (Figure 18: BlM/BrM). This coupling occurs several times throughout the core, and the transition between these facies is always very abrupt, with a stark, immediate change from one to the other and back (Figure 23). The core then is overlain by the fissile facies from 11,843’06” until 11,842’05” (Figures 17 & 21: BBF/BBFD). There is a brief transition back to the consolidated facies before a gap in the core at 11,842”.

Above the break, there is a short fissile interval (Figure 20: BlF) after which the core becomes dominated by a dolomite-rich unit from 11,840’03” to 11,835’ (Figure 24, Figure 19: DDFML/DDFMD). This unit differs from the dolomite rich facies in the previous core in that it lacks the pockets of sand, but contains coarse skeletal fragments of organisms including, but not limited to crinoid stem pieces and shell fragments throughout much of the unit (Figures 19 & 20: DDFCL/DDFCD). Much of the sediment, particularly that which contains the coarse fragments, appears to have been reworked. Within this dolomite-rich unit, there are distinctly light-colored and dark-colored facies.

Above the dolomite-rich unit, the core alternates between consolidated black and brown massive mudrock facies (Figure 18: BlM/BrM) roughly every six inches with occasional laminations throughout. There are isolated pockets of grey sand within this section of the core. This continues until 11823' when the core returns to a fissile facies (Figures 17 & 20: BlF/BBF).

While fractures in the previous core were limited to the nodules, they are abundant throughout the Velma core. The dolomite unit contains a high density of crystal filled fractures running throughout. In the rest of the core, the fissile, clay-rich facies appear to have served as planes of weakness, with slickensides being common throughout. Although slickensides were more common within the clay-rich facies, they were not restricted exclusively to these facies. Additionally, while the Boatwright core contains a good deal of pyrite, it is not present to nearly the same degree within the Velma core. A detailed core description at a one inch resolution with facies codes and data visualization can be found in appendix B.

Figure 22. Clay-rich base of Velma core. Depth interval 11,849'-11,854'11".

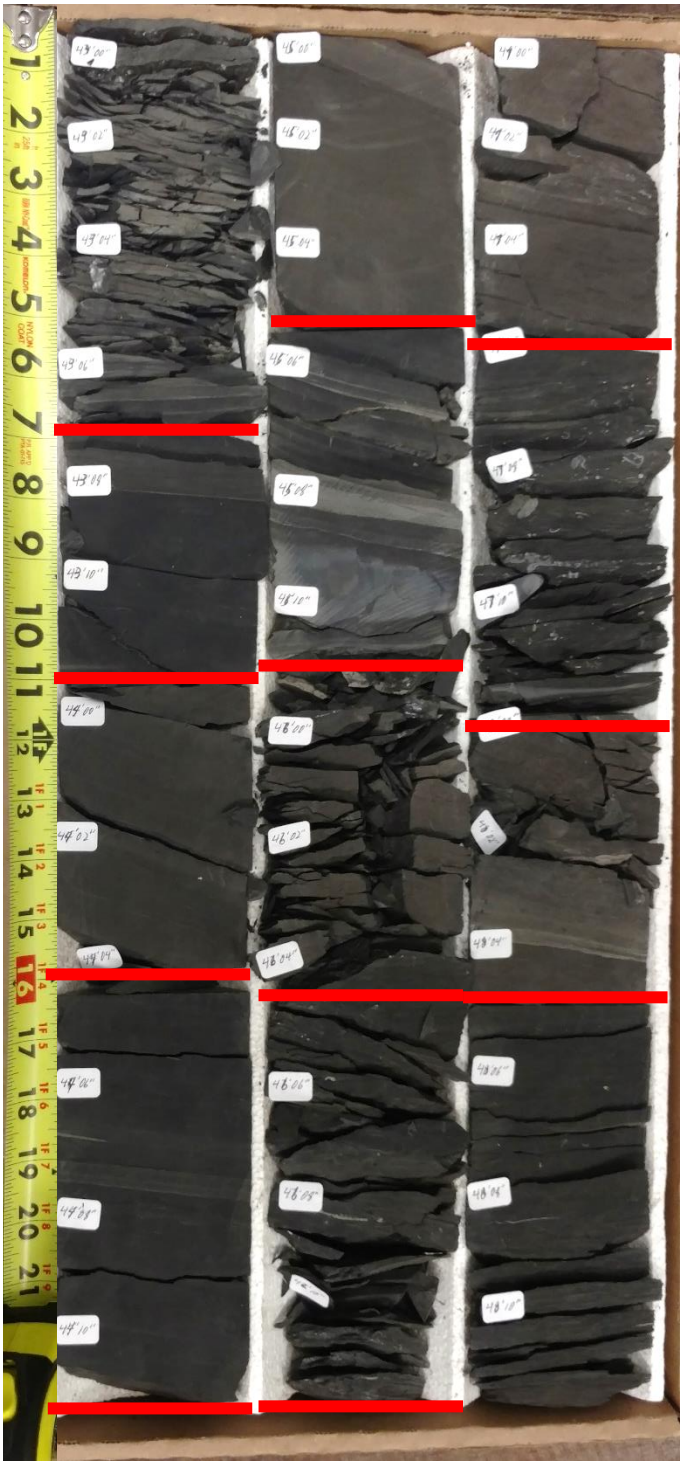

Figure 23. Rapid facies shifts between brown and black mudrocks in Velma core between 11,845'10" and 11,843'06". Red lines indicate facies shifts.

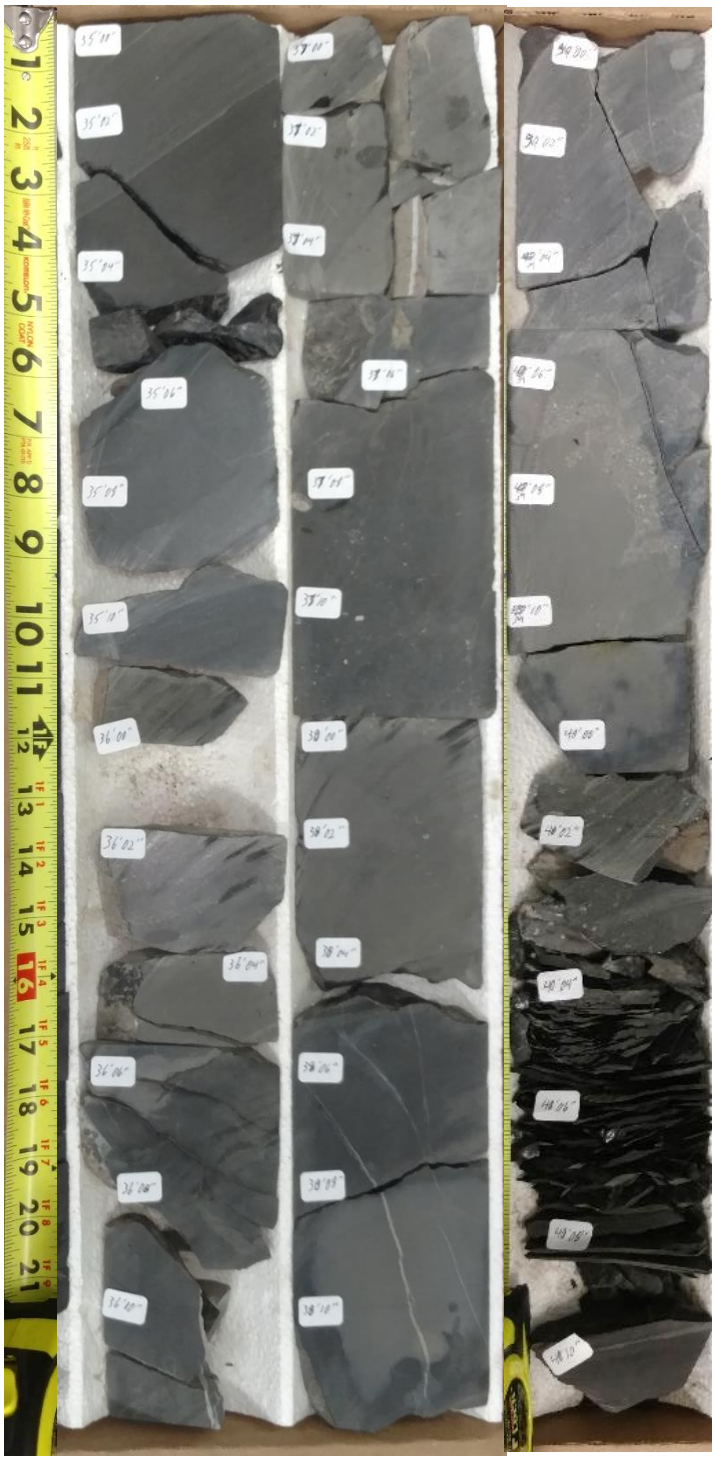

Figure 24. Dolomitic section within Velma core between 11,835’ and 11,840’.

3.2 X-RAY DIFFRACTION

X-ray diffraction analysis was provided for the each core, and results were consistent with the observations made in the description. The formation overall is siliceous-argillaceous, with the exception being the dolomite beds (Figures 25 & 26). The argillic content largely consists of coupled illite/smectite and illite with associated micas. Within the Boatwright core, the X-ray diffraction indicates a clay rich base followed by a sharp increase in the quartz content beginning at 13,052'. Shortly into this quartz-rich unit there is a unit dominated by dolomite. The quartz content gradually decreases upwards in the core until the upper section in which quartz content and clay content fluctuate more rapidly (Figure 27).

The Velma core is similar in its siliceous-argillaceous composition, again with exceptions made within dolomite beds. The predominant clay minerals are again illite/smectite followed by illite with associated micas. The base of the core contains a greater clay content than the upper units. Following the dolomite bed, there is a sharp increase in the quartz content that gradually decreases upsection (Figure 28). Given the resolution of the data available, it is unlikely that this dataset captures the variability of the facies in their entirety, as the Velma core often exhibits facies changes on the scale of every 6-8 inches.

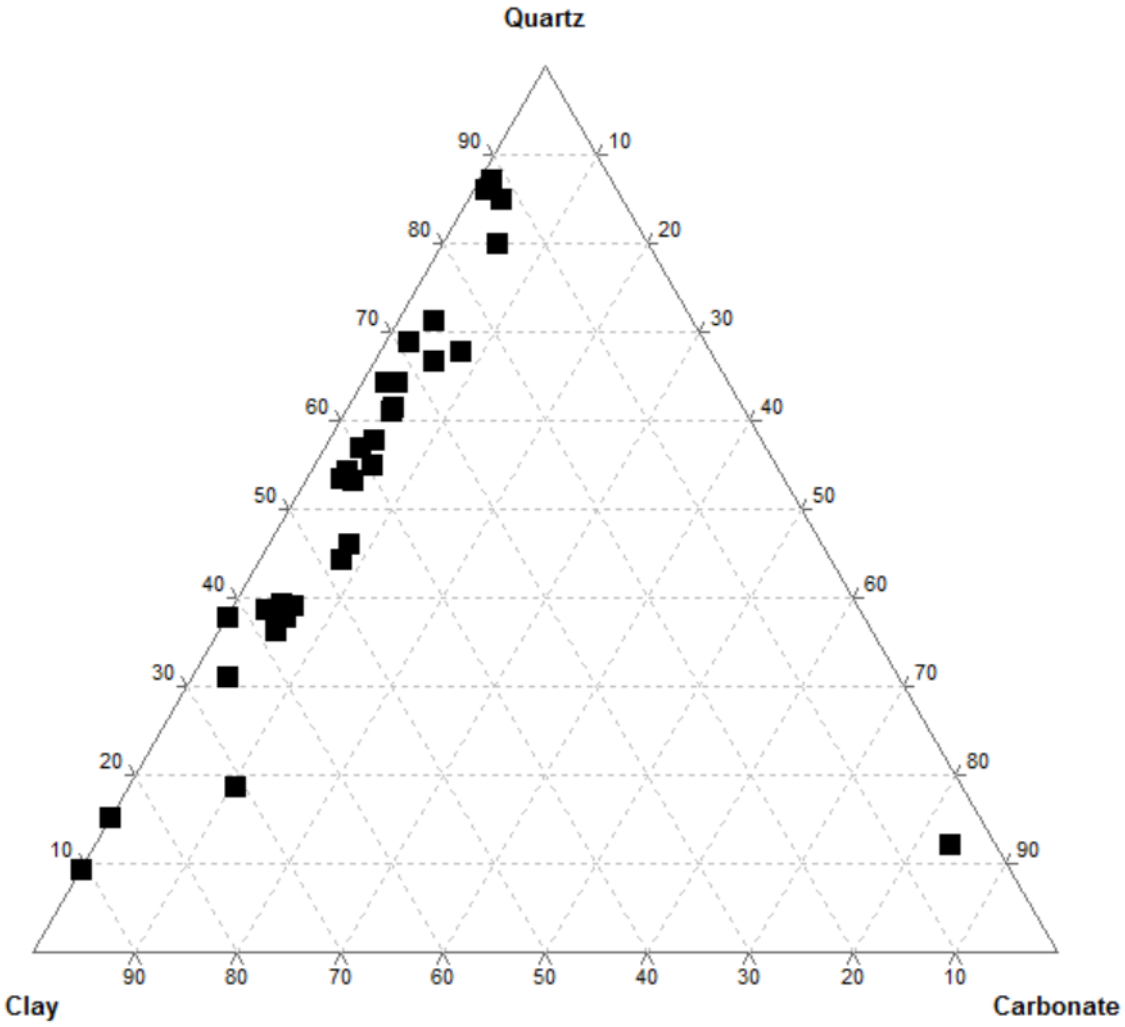

Figure 25. Ternary diagram demonstrating relative abundances of quartz, clay minerals, and carbonate minerals in the Boatwright core. Note the overall trend being siliceous-argillaceous, with a single carbonate rich outlier which is the dolomite bed.

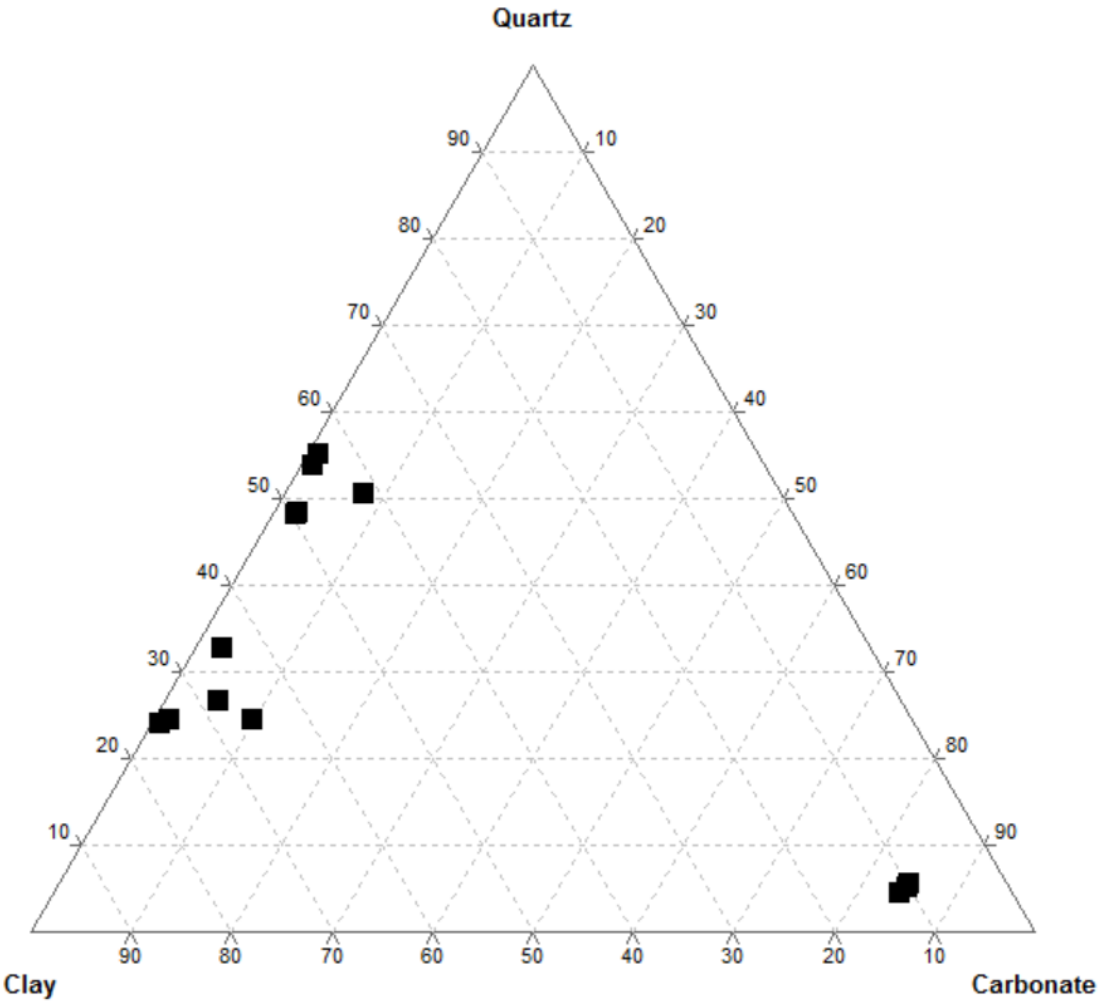

Figure 26. Ternary diagram demonstrating relative abundances of quartz, clay minerals, and carbonate minerals in the Velma core. Again, note the overall trend being siliceous-argillaceous, with carbonate outliers within the dolomite bed.

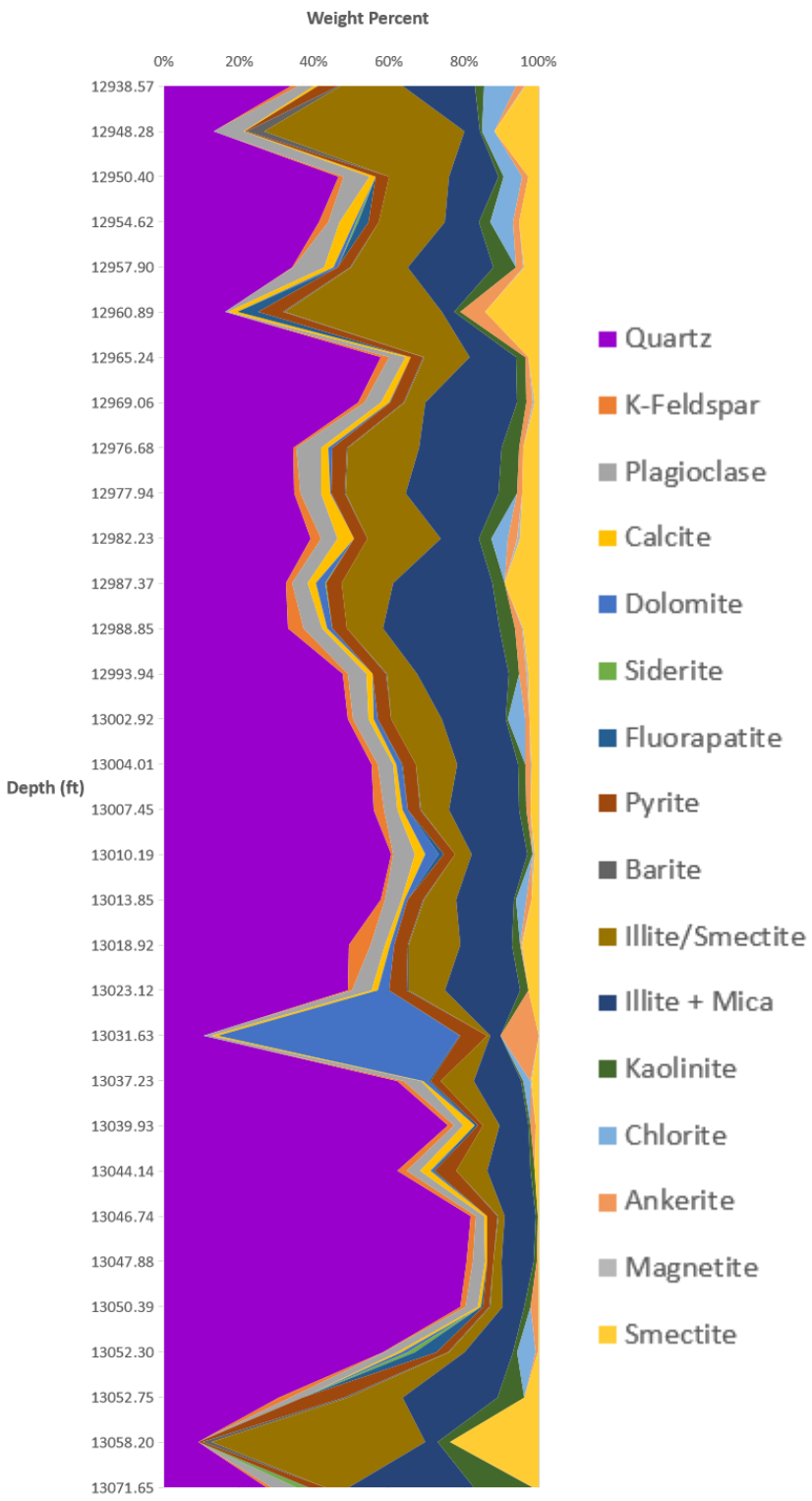

Figure 27. XRD mineralogy of Boatwright core.

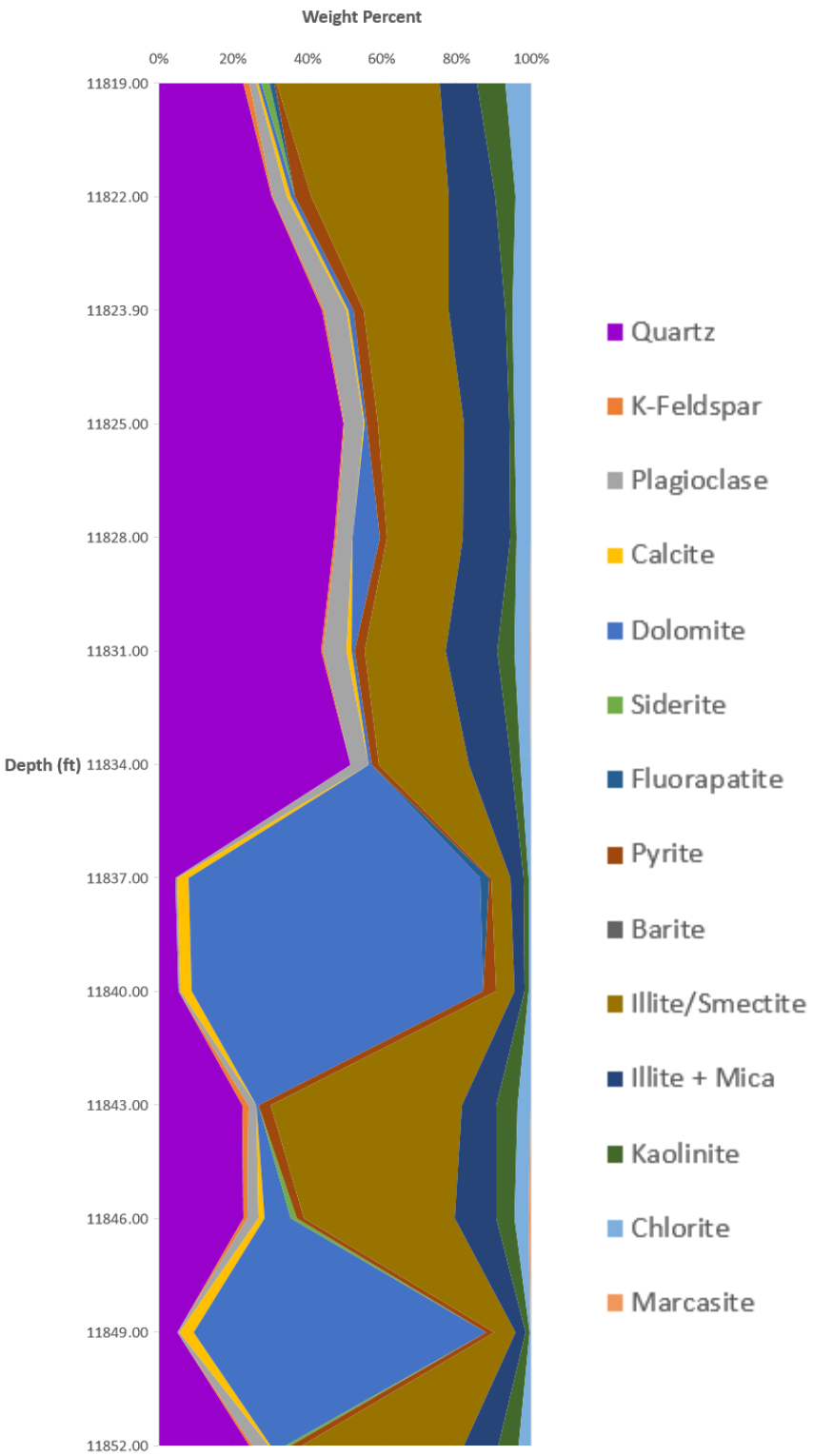

Figure 28. XRD mineralogy of Velma core.

3.3 CHEMOSTRATIGRAPHY

3.3.1 Chemostratigraphic Trends

The XRF profile for the Boatwright core can be seen in figure 29. The base of the Boatwright core begins with a unit that is very high in aluminum, with around 75,000 ppm on average. There are many points at which the aluminum levels will abruptly drop. These data points are associated with nodules, and coincide with spikes in phosphorous, calcium, magnesium, and strontium as well as silicon/aluminum and silicon/titanium ratios. In the lower section of the core, these dips coincide with iron, likely due to pyrite content within the nodules. Potassium, thorium, titanium, rubidium, and zircon all track well with aluminum. (Figure 29) The high aluminum content abruptly stops at 13052’08” when the core transitions into less fissile facies. At this transition, the silicon to aluminum ratio as well as the silicon to titanium ratio experience a marked increase from around 2 for silicon/aluminum and around 40 for silicon/titanium before returning to a higher baseline value of around 5 for silicon/aluminum and 120 for silicon/titanium that gradually declines throughout much of the core; however, as noted, this baseline is still higher than that present in the lowermost facies. From 13033’ to 13030’07”, the core exhibits a sharp increase in calcium and magnesium levels associated with the dolomite-rich facies.

Regarding anoxia proxies, molybdenum levels are fairly constant throughout the core, remaining around 30 ppm with slightly higher levels existing above the transition from the fissile facies at the base to the more consolidated facies present in the rest of the core. There is a single spike in molybdenum values at 12,958’06” that coincides with increases in sulfur, uranium, copper, and zinc. Vanadium levels demonstrate a

much more noticeable shift from the lower facies to the upper facies. In the lower facies, vanadium has a fairly low baseline value, generally around 75 ppm, marked by occasional spikes. After the transition, the baseline value is consistently higher than 150 ppm, with some degree of cyclicity becoming evident. Vanadium reaches its highest values towards the top of the core, with consistently high values between 12967’ and 12963’ with the exception of a nodule, reaching its highest point at 740.35 ppm. This section coincides with elevated uranium levels as well as a marked decrease in aluminum, potassium, thorium, titanium, rubidium, and zircon, and somewhat coincides with a slightly elevated silicon to titanium ratio. This trend is repeated to a lesser degree from 12937’ to 12943’. Overall, vanadium tends to increase with decreases in aluminum content. Uranium levels are erratic throughout the core, maxing out at 30 ppm, although they are noticeably higher in the upper facies than in the lower facies.

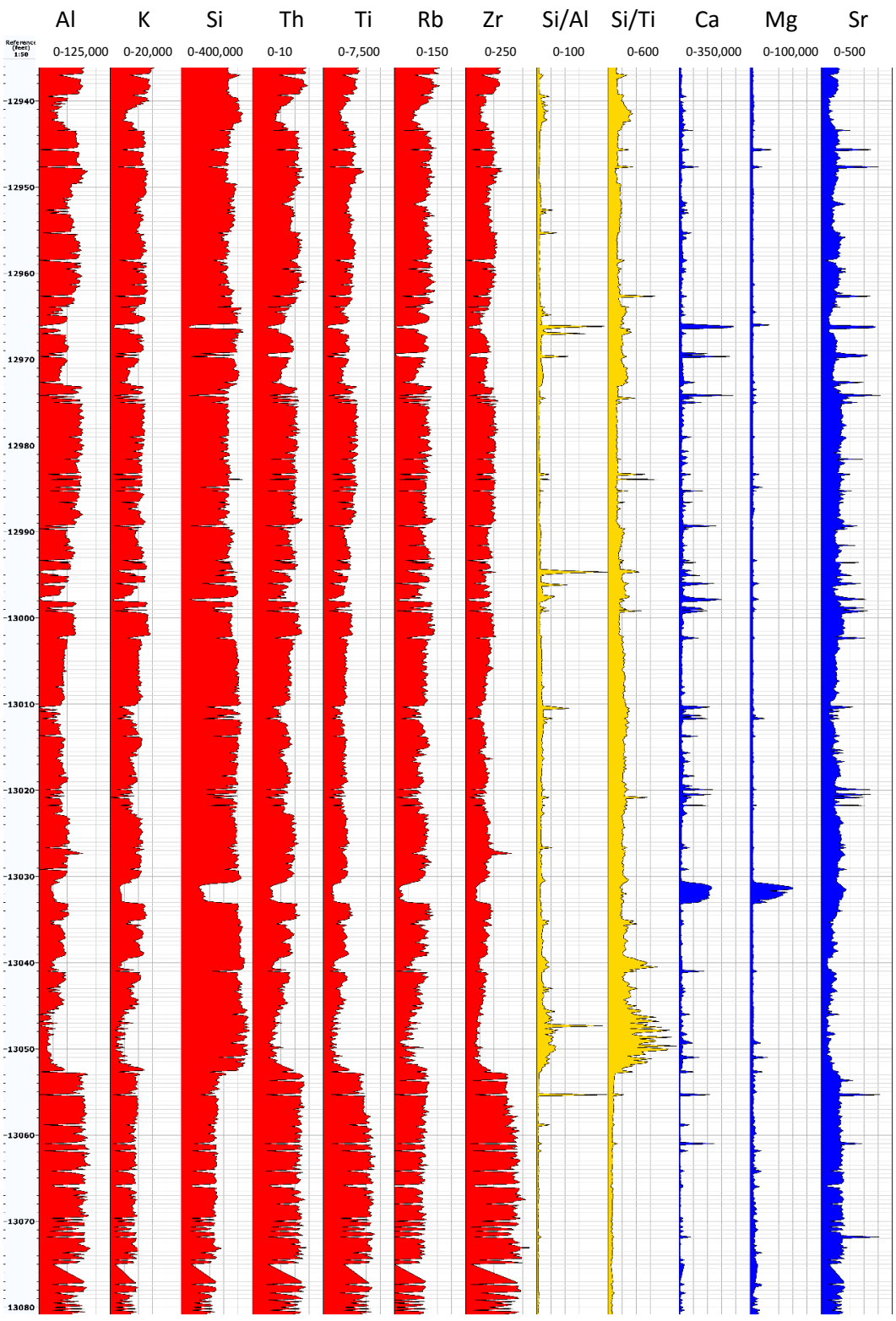

Figure 29. Chemostratigraphic columns from Boatwright core. Clay and continental proxies are in red. Ratios of Silicon to Aluminum and Titanium indicate relative terrigenous input and are in yellow. Carbonate proxies are in blue. All units in ppm.

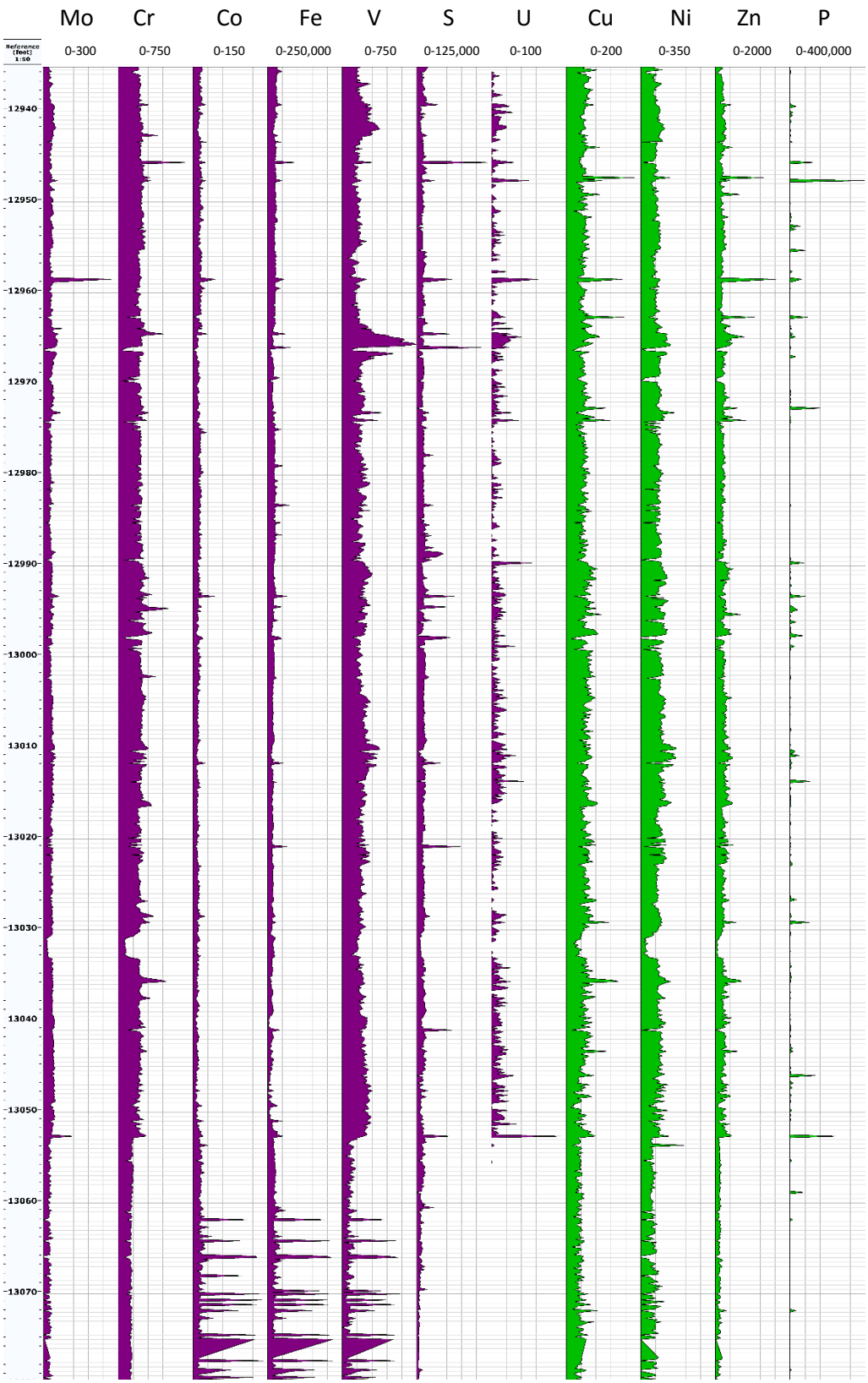

Figure 29. Chemostratigraphic columns from Boatwright core. Anoxia proxies are in purple. Productivity proxies are in green. All units in ppm.

The XRF profile for the Velma core can be seen in figure 30. The base of the Velma core is also rather aluminum rich, with around 100,000 ppm aluminum from its base at 11,854’ until 11,845’ 10”. As was in the Boatwright core, potassium, thorium, titanium, rubidium, and zircon all track well with aluminum. (Figure 30) At this point, there is an increase in the calcium and magnesium content, reaching a combined total as high as 200,000 ppm. The carbonate proxies briefly decline as the aluminum content increases until 11,840’03” whereupon the carbonate proxies range between 250,000-320,000 ppm. This trend continues until 11,835’05”. This calcium and magnesium rich zone marks a shift in the core. Below this zone, silicon has a baseline of around 240,000 ppm. Following this transition, silicon jumps to 320,000 ppm before gradually declining back to around 240,000. Silicon/aluminum and silicon/titanium ratios nearly double in the section above the calcium-dolomite zone, compared to the zone below, going from roughly 5 to about 10 in the silicon/aluminum ratio and from about 50 to about 100 in the silicon to titanium ratio. There are several spikes in these values which generally coincide with elevated calcium and magnesium levels; however, the greatest increase occurs at 11,833’ which does not coincide with a proportional increase in calcium and magnesium levels. Additionally, in the large calcium-magnesium rich zone, there is not an increase in silicon/aluminum and silicon/titanium ratios as there is elsewhere in the core. Furthermore, there is an apparent cyclical trend that is most evident within the aluminum content. From the base of the core, moving up-section into the calcium-magnesium rich zone, there is a decrease in the aluminum content. Moving up-section from this zone, the aluminum content begins to gradually increase again to nearly 100,000 ppm. There exist intermittent decreases in the aluminum content, and these

coincide with increases in calcium and magnesium, as well as spikes in silicon/aluminum and silicon/titanium ratios.

Regarding anoxia proxies, values for molybdenum, chromium, and vanadium are all slightly lower than those seen in the Boatwright core; however there are no real spikes in concentrations and no clear trends present save for a decrease in molybdenum and chromium associated with the calcium-magnesium rich zone. Curiously, there is a single spike in uranium within this zone.

Regarding proxies for productivity, there is an apparent inverse relationship between calcium/magnesium and copper, nickel, and zinc. Phosphorous is very lacking in the Velma core compared to the Boatwright.

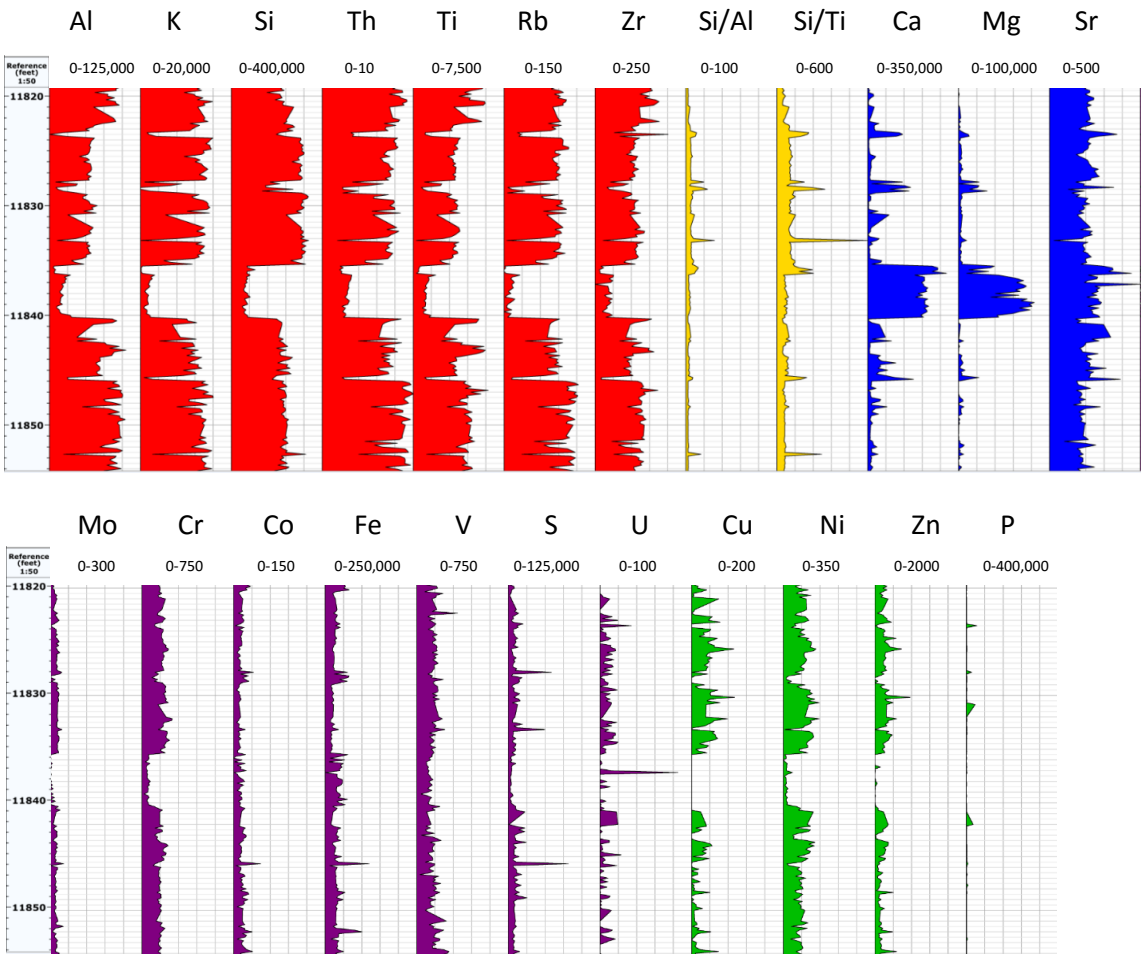

Figure 30. Chemostratigraphic columns from Velma core. Clay and continental proxies are highlighted in red. Ratios of Silicon to Aluminum and Titanium indicate relative terrigenous input and are highlighted in yellow. Carbonate proxies are highlighted in blue. Anoxia proxies are highlighted in purple. Productivity proxies are highlighted in green. All units in ppm.

While there are no strong correlations relating to anoxia proxies and elements detectable by a spectral gamma ray log (uranium, thorium, potassium), each core demonstrated a strong correlation between titanium and thorium levels. (Davis 2015) (Figure 31) Titanium being a continental proxy, tracks well with clay content. Therefore, while there is no means by which to directly find zones of high brittleness and organic content by means of spectral gamma ray log, it is possible to eliminate the more ductile, organic-poor zones which contain a high degree of continental input by their relatively high thorium content. Additionally, the zones with the highest argillic content do not fit within the linear trend of the core as a whole. In each core, there appears to be an upper limit for thorium, yet the titanium content continues to grow. Nevertheless, the high values of thorium are associated with high titanium values. There is merely a point at which continental input beyond a certain point may not be accurately predicted based upon thorium levels. Furthermore, this trend does not apply to nodules within the formation. They do not exhibit any clear trend in this regard, and introduce noise into the data.

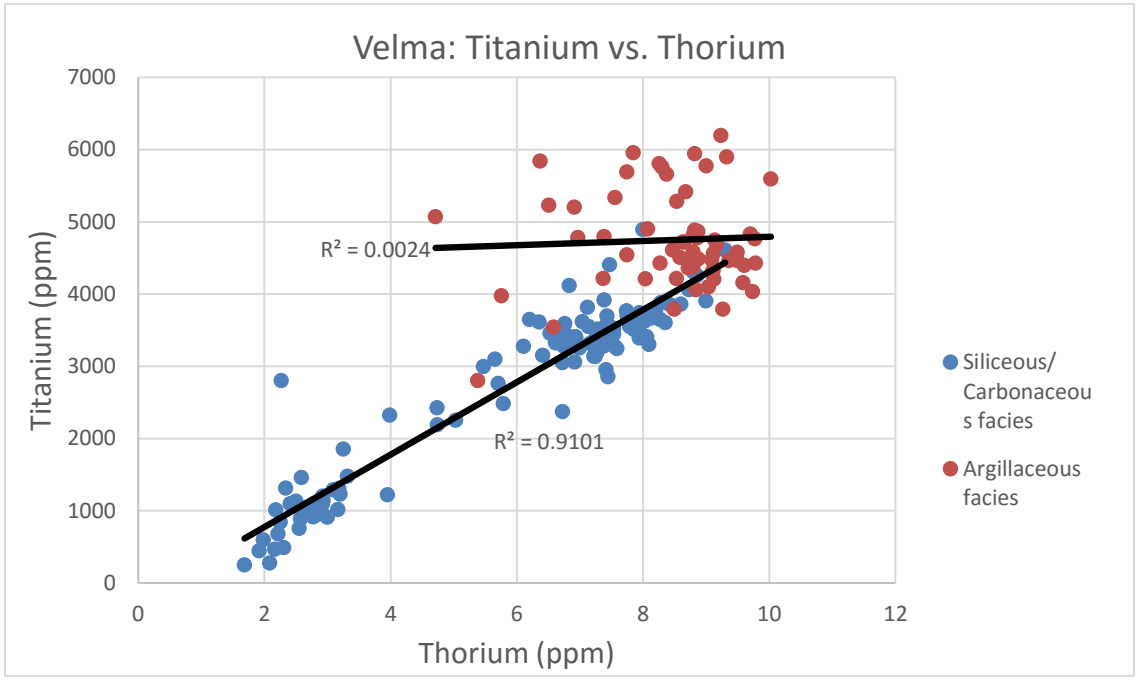

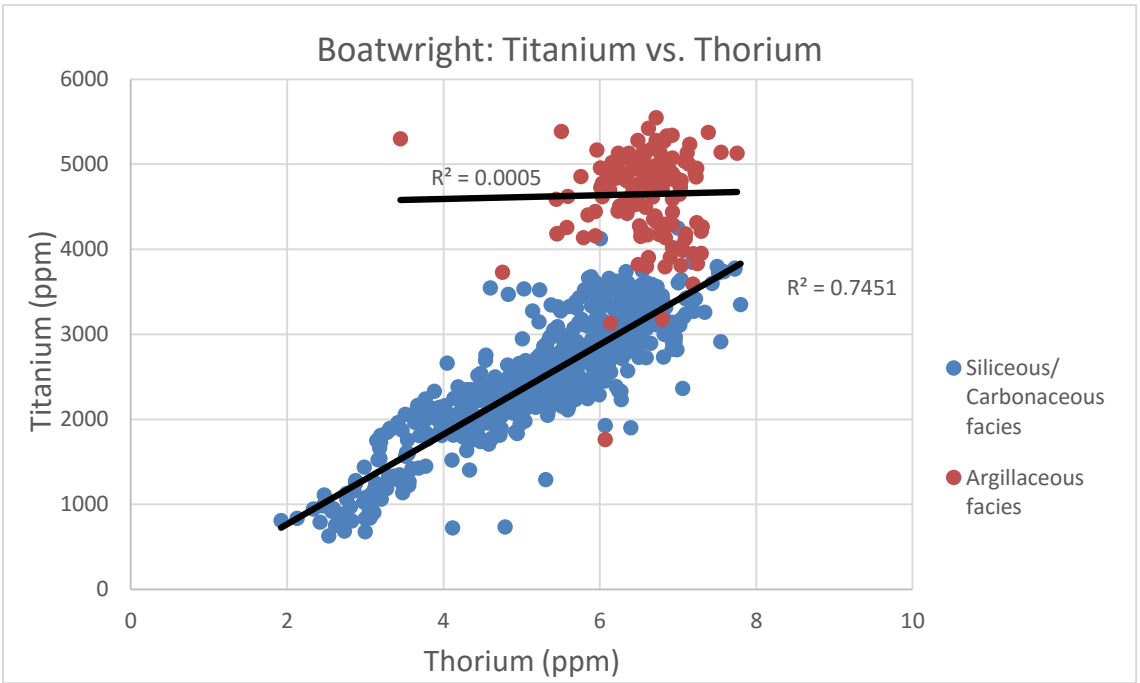

Figure 31. Scatterplots demonstrating relationship between titanium (y-axis) and thorium (x-axis). Red values are associated with clay-rich facies, and blue values with more siliceous or carbonate-rich facies. Nodules were omitted from these plots. Each core demonstrates a correlation between thorium and titanium in all but the most argillaceous facies.

3.3.2 Chemofacies

Despite the greater number of lithofacies within the Velma core, a greater number of chemofacies were identified in the Boatwright, although the number was not significantly greater with the Boatwright containing 11 chemofacies and the Velma core containing 10.

Table 4. Chemofacies within the Boatwright Core

1	Low Silicon/Aluminum ratio
2	High Calcium, elevated Magnesium and Silicon/Aluminum ratio
3	Elevated Uranium and Vanadium
4	High Phosphorus, Calcium, Silicon/Aluminum ratio, and Uranium
5	High Silicon/Aluminum ratio, low Titanium and Zircon, elevated Uranium, Molybdenum, and Vanadium
6	High Uranium and Vanadium
7	Moderate Silicon/Aluminum ratio
8	Very high Phosphorus and high barium
9	Low Silicon/Aluminum ratio, elevated Titanium and Zircon
10	High Magnesium and Calcium
11	High Iron, Vanadium, Manganese, and Cobalt

Table 5: Chemofacies within the Velma Core

1	Low Silicon/Aluminum ratio
2	Low Silicon/Aluminum ratio, high Barium
3	Slightly lowered Silicon/Aluminum ratios, elevated Nickel
4	Elevated Silicon/Aluminum ratio, high Copper, elevated Nickel
5	High Calcium, Magnesium, and Silicon/Aluminum ratios
6	Very high Phosphorus and high Uranium
7	High Silicon/Aluminum ratios, Sulfur, Phosphorus, Magnesium
8	High Titanium
9	Very high Magnesium
10	High Strontium

While there is no direct correlation between chemofacies and lithofacies, there are identifiable trends. The low Silicon/Aluminum ratio chemofacies are associated with the more fissile, clay-rich lithofacies; high Silicon/Aluminum ratio chemofacies are associated with the more quartz-rich lithofacies; high Magnesium and Calcium chemofacies are associated with dolomitic lithofacies, and high Phosphorus chemofacies are associated with nodules and apatite-rich lithofacies. It is worth noting that within the Velma core, chemofacies 8 and 10 are outliers, each containing a single data point, which had a high level of dissimilarity to all other clusters. Additionally, chemofacies 1 and 2 are very similar, but 2 contained a high level of Barium. This may be due to the difficulty of cleaning this section of the core owing to its highly fissile

nature, leading to drilling mud contamination. Distribution of chemofacies can be seen in figures 32 and 33.

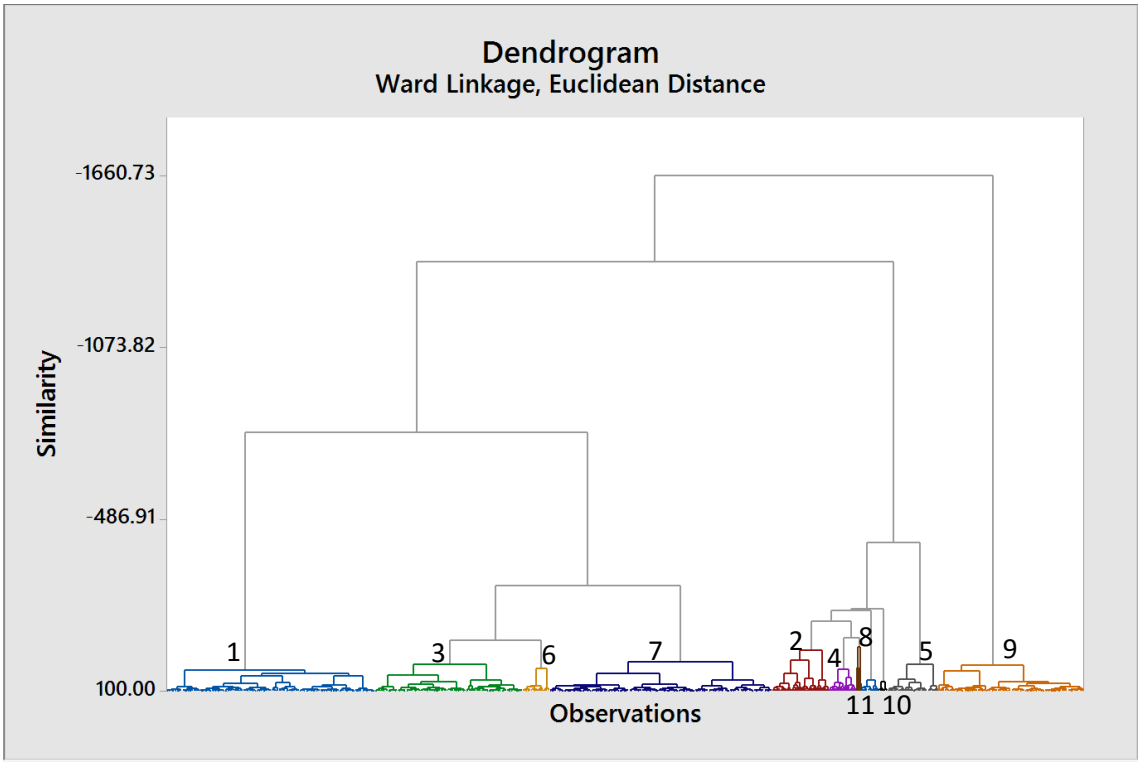

Figure 32. Dendrogram of chemofacies within the Boatwright core. Numbers indicate which cluster listed above each branch corresponds to. Note the small size of 8, 10, and 11 and their relatively high level of dissimilarity with other chemofacies.

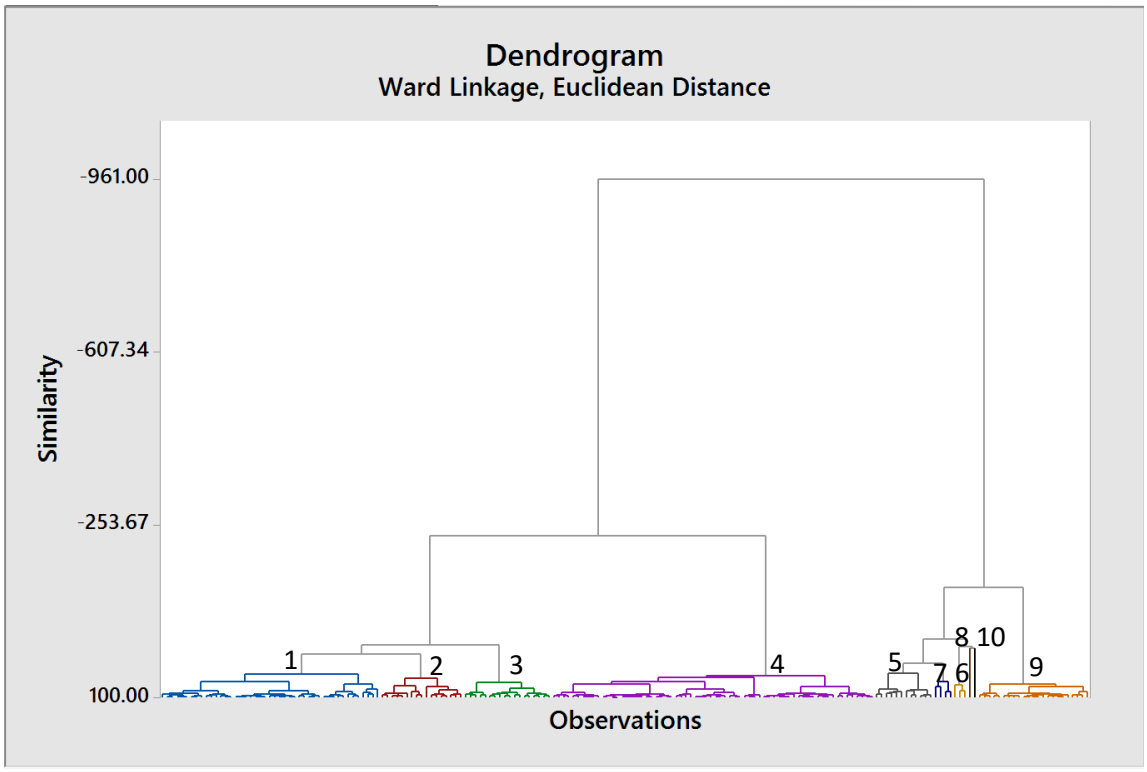

Figure 33. Dendrogram of chemofacies within Velma core. Numbers indicate which cluster listed above each branch corresponds to. Both 8 and 10 represent single data points that did not fit into any other categories.

From the base of the core until 13,052’08”, the Boatwright core is comprised primarily of chemofacies 9, which is defined by its low silicon/aluminum ratio and elevated levels of titanium and zirconium, indicating a high clay content and high degree of continental input (Figure 34). This is the only part of the core that contains this chemofacies, except for a single data point at 12,984’10”. This interval is punctuated by nodules marked by high levels of iron, vanadium, manganese, and cobalt, placing them within chemofacies 11. These nodules are not present in any other section of the core. All other nodules fall within chemofacies 2, which contains high calcium and elevated magnesium levels, or chemofacies 4, which contains high phosphorous levels. There is no clear divide between a section of the core containing one or the other. At the transition, there is a single interval of chemofacies 8, defined by high phosphorous and barium levels. Following the transition, until 13,045’04” the core is dominated by chemofacies 5, defined by a high silicon/aluminum ratio, an elevated concentration of redox associated elements, and a low concentration of continental proxies, indicating a high biogenic quartz content. Although there are occasional instances in which this chemofacies reappears, it is never as continuous as it is in this lower section following the transition. Moving upsection from this, there is a shift to chemofacies 3 until 13,042’02” in which the core contains slightly elevated uranium and vanadium levels, proxies for anoxia. Following this, from 13,042’02” until 13,002’, the core is primarily made up of chemofacies 7, defined by its moderate silicon/aluminum and silicon titanium ratios. This section is punctuated by intervals of chemofacies 3. A notable exception in this zone being the dolomite rich interval between 13,032’06” and 13,031’, which was comprised of chemofacies 10. After

13,002', while chemofacies 7 remains an important constituent of the core, the primary chemofacies becomes chemofacies 1, defined by its low silicon/aluminum ratio, albeit not as low as that of chemofacies 9.

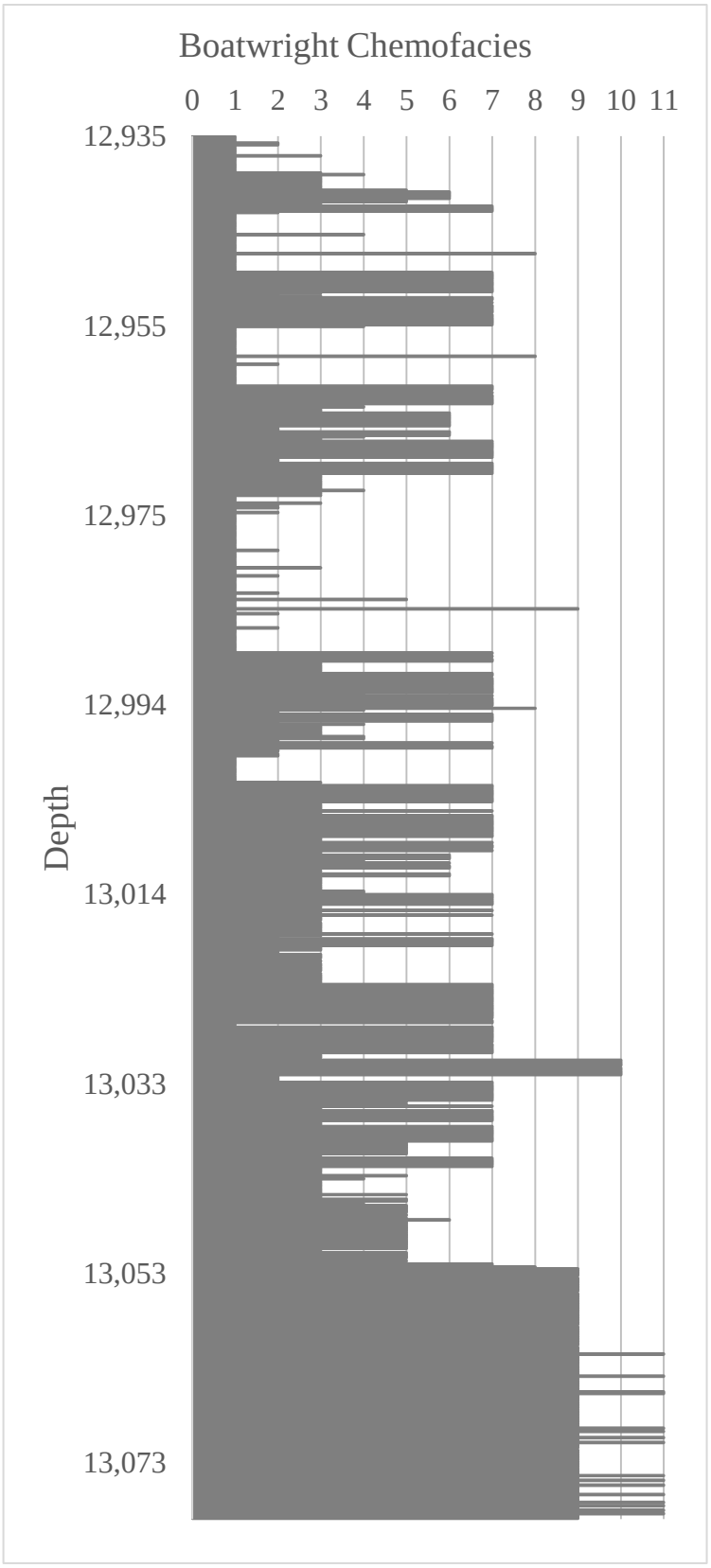

Figure 34. Distribution of chemofacies within Boatwright core.

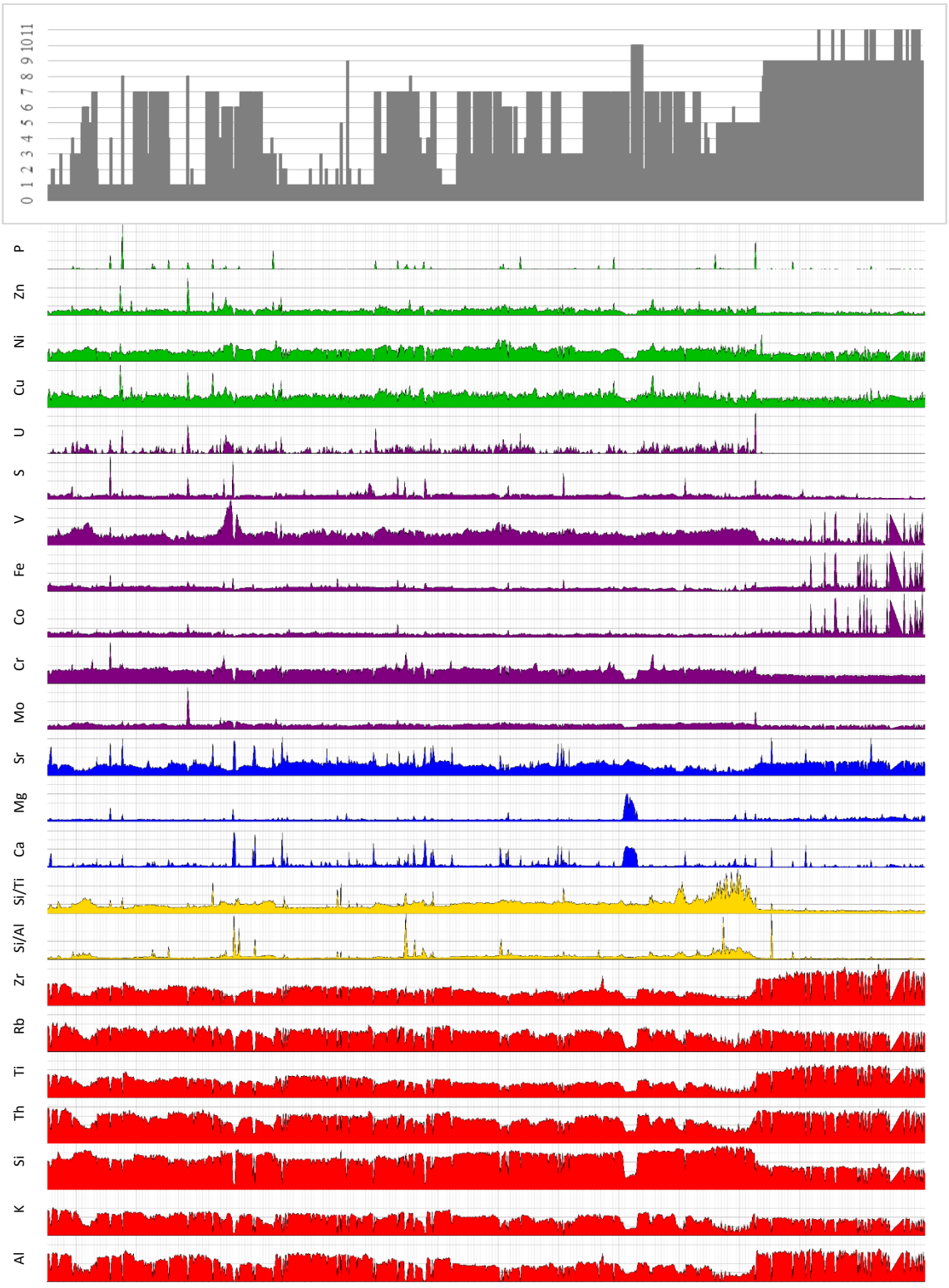

Figure 35. Comparison of chemofacies and chemostratigraphic trends in Boatwright core.

The base of the Velma core is comprised primarily of chemofacies 1, defined by its low silicon/aluminum and silicon/titanium ratios (Figure 36). It is occasionally punctuated by chemofacies 2, which has a very similar makeup, except for its high barium levels. It is likely that chemofacies 2 is the result of drilling mud contamination within chemofacies 1. At 11,845'06", the core shifts to being dominated by chemofacies 3 and 4. Chemofacies 3 is defined by slightly lowered silicon/aluminum and silicon/titanium ratios and elevated nickel. Chemofacies 4 is defined by elevated silicon/aluminum and silicon/titanium ratios as well as elevated nickel levels and high copper levels. This is demonstrating an overall increase in proxies for productivity as well as an increase in biogenic silica content, with higher productivity levels within chemofacies 4. The core is dominated by chemofacies 9 from 11,840'02" to 11,836'04" within the dolomite horizons. This chemofacies is defined by high calcium levels and very high magnesium levels. Following this section, there is a transition zone that extends until 11,835'06" marked by chemofacies 5, which has similar calcium and magnesium levels, but is also accompanied by high silicon/aluminum and silicon/titanium ratios indicative of a higher degree of biogenic silica production. Following this, the core is defined primarily by chemofacies 4 until 11,824'. Following this fairly homogeneous chemofacies unit, there are a number of rapid changes in the remainder of the core. A different chemofacies is recorded at nearly every measurement, with an overall trend of decreasing silicon/aluminum and silicon/titanium ratios. However, there is no clear representation of these rapid changes within the lithofacies.

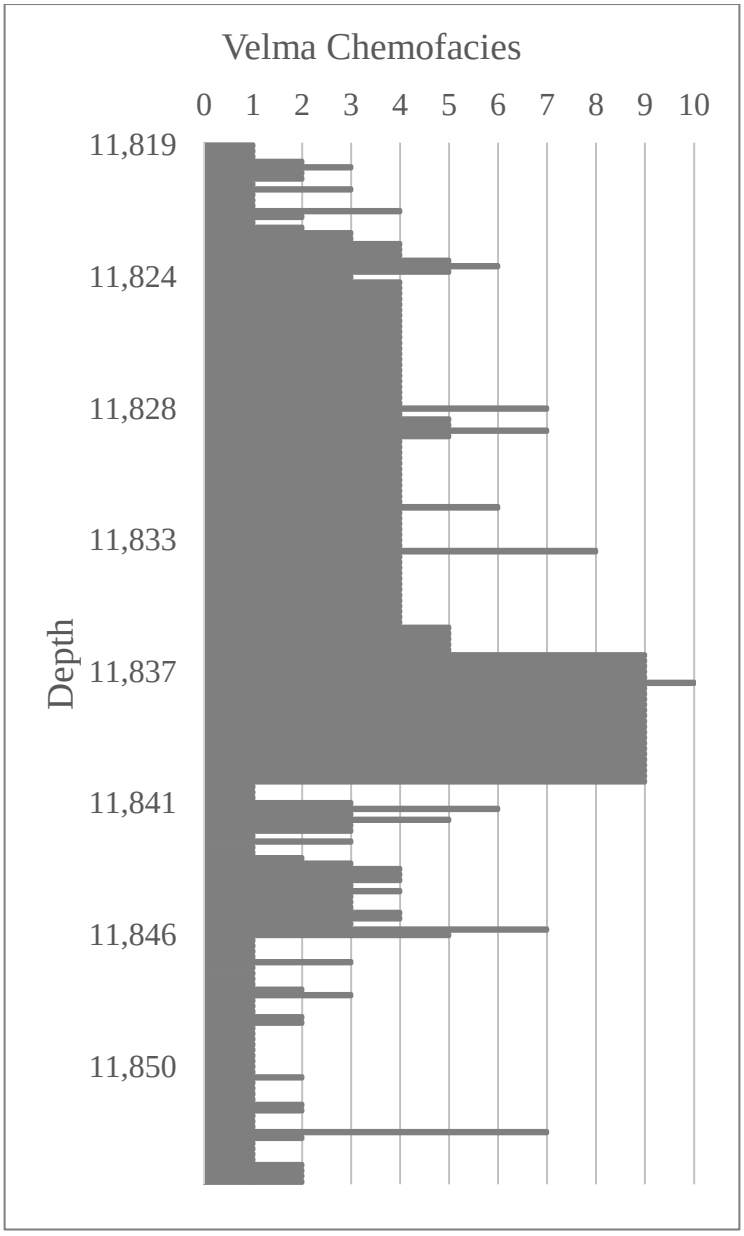

Figure 36. Distribution of chemofacies within Velma core.

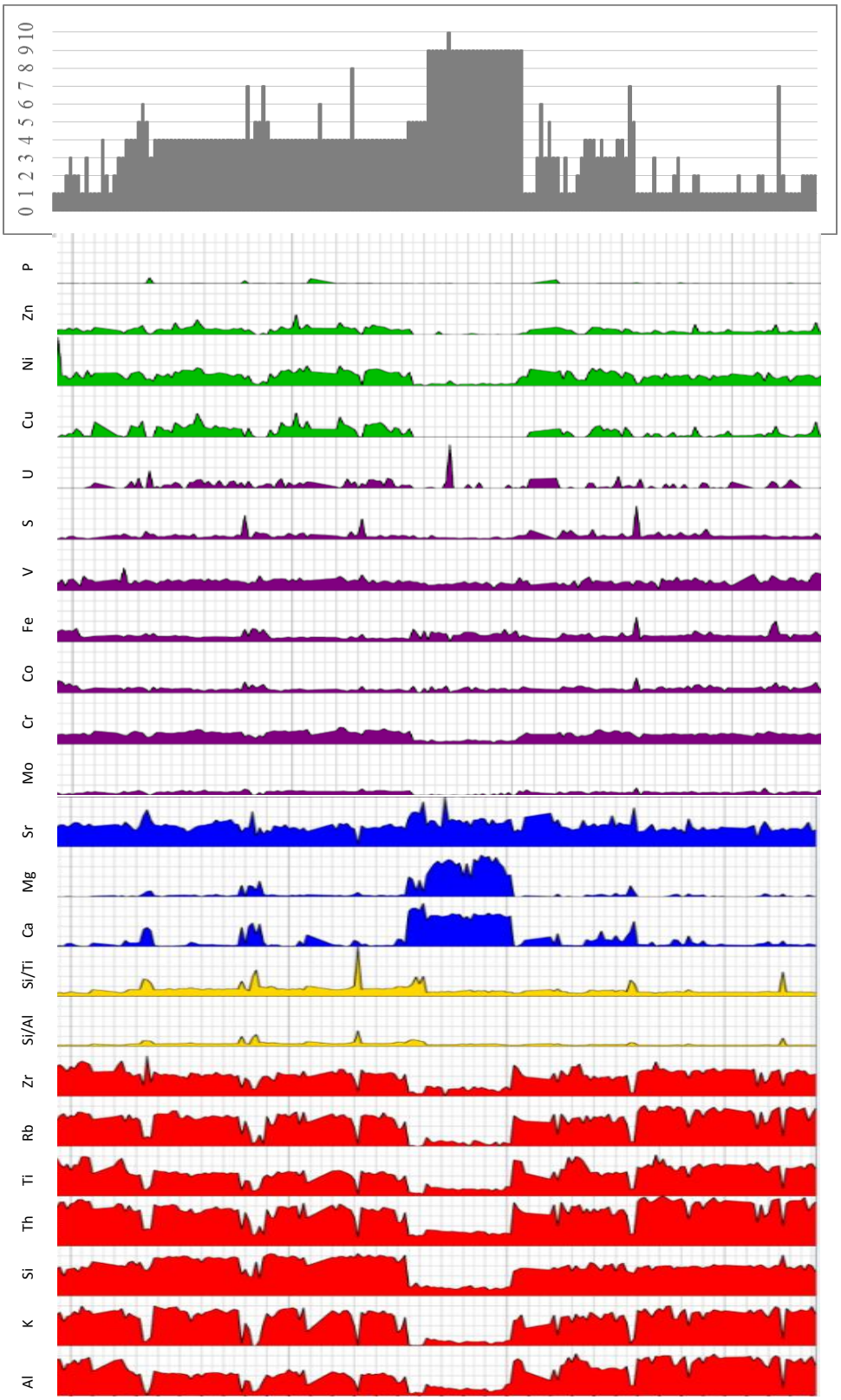

Figure 37. Comparison of chemofacies and chemostratigraphic trends within the Velma core.

3.4 HARDNESS TESTING

Hardness values were obtained on the Velma core via rebound hammer testing using the Proceq Equotip Piccolo 2^{TM}. Rebound hammer tests give a unitless measurement of the hardness of the rock, with higher values indicating a rock's propensity to fracture rather than deform plastically. Hardness values measured in the core can be seen in figure 38. Lower values are associated with the clay-rich units within the core. In many instances, the clay rich units lack any sort of measurement due to their high friability preventing the acquisition of any meaningful readings. Trends observed within the values obtained mirror those seen in the chemostratigraphy. From the base of the Velma core until 11,841', values typically fall between 200 and 400, gradually increasing moving upsection. The values are consistently high within the dolomite rich beds, typically measuring above 500. Apart from the large dolomite bed located between 11840'03" and 11835'05" there are additional spikes located at 11,823' and 11,828', which can be seen to have elevated levels of calcium and magnesium in XRF; although they lack the level of dolomite present within the larger bed and do not have a similar appearance in the core. An additional spike can be seen at 11,833' which coincides with a high silicon/titanium ratio, indicating a high biogenic quartz content. Following the dolomite rich bed, apart from the aforementioned exceptions, there is a general trend of a decrease in hardness values, which is consistent with the increase in aluminum values seen in XRF.

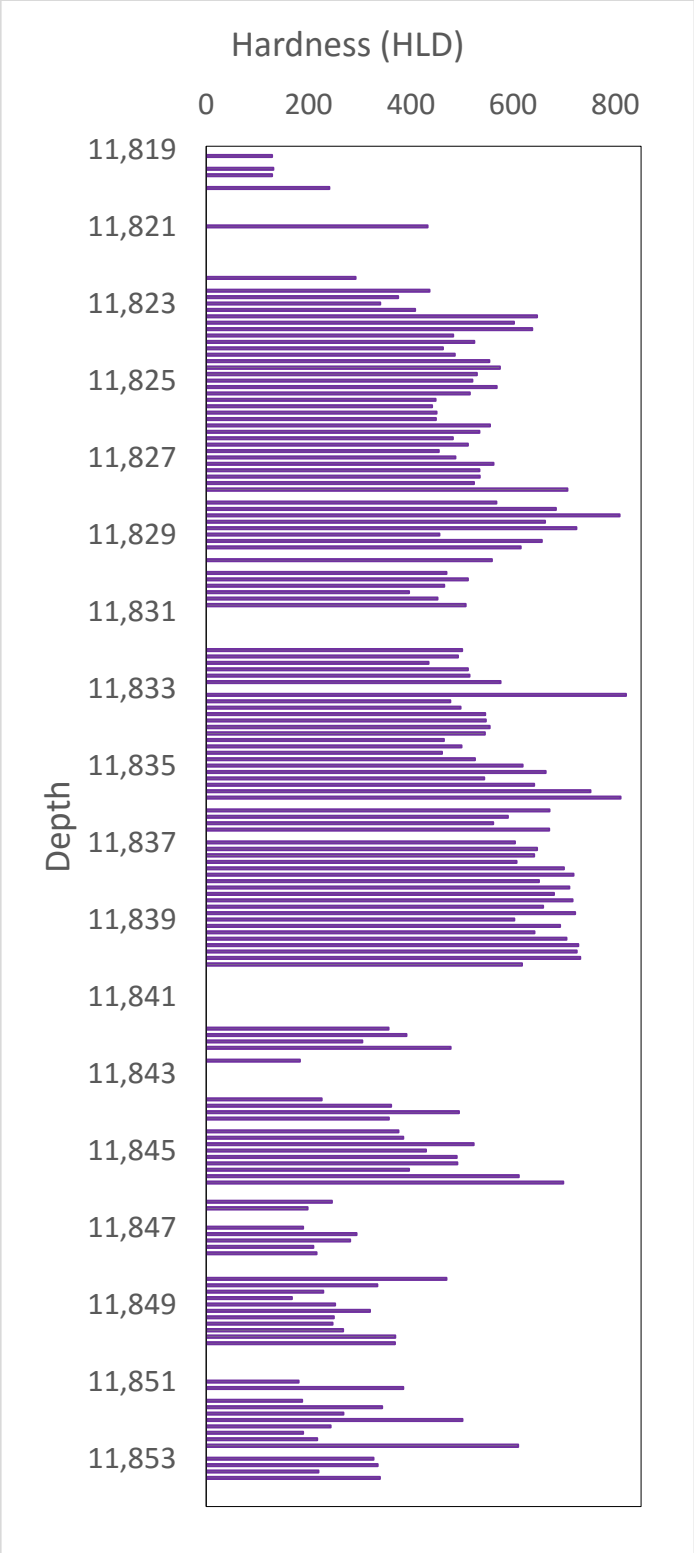

Figure 38. Rebound hammer results from Velma core. Gaps in data are due to missing core sections or facies that were too fissile to conduct testing on. Higher values indicate more brittle facies.

3.5 POROSITY

3.5.1 Broken Surfaces Technique

All porosity values were obtained from sidewall core samples taken outside of the depth intervals of the cores described. Therefore, they cannot be definitively tied to any of the lithofacies or chemofacies described. Porosity values obtained from the technique utilizing SEM imaging of freshly broken surfaces range from 7.04% to 13.11%. The full range of values can be seen in Table 6. Of particular note is the relatively high amount of porosity present along the bedding planes, i.e. the "top" of each sample. Typically porosity seen in this orientation is greatly reduced due to the platy nature of clay minerals. (Slatt et al. 2013) The high degree of porosity in this orientation could contribute to a greater interconnectivity of pores across bedding planes, and in turn a higher permeability in the formation.

Table 6: Broken Surfaces Technique Porosity Values

Sample		TOTAL%	<1um length	>1um length	
			%por	%por	Ratio
12394	Front	10.72	8.78	1.93	
	Side	9.34	8.05	1.29	
	Top	7.46	6.31	1.15	
	Average	9.17	7.71	1.46	5.30
12469.5	Front	10.08	8.36	1.72	
	Side	6.22	5.16	1.06	
	Top	9.30	7.32	2.37	
	Average	8.53	6.95	1.72	4.00
12555	Front	8.67	6.88	1.79	
	Side	5.39	4.35	1.04	
	Top	7.07	5.89	1.18	
	Average	7.04	5.71	1.34	4.20
12593	Front	12.60	10.41	2.33	
	Side	13.233	11.01017	2.715594	
	Top	13.50	10.83	2.41	
	Average	13.11	10.75	2.48	4.30
12618	Front	9.278	7.551373	1.726627	
	Side	11.263	8.977241	2.295759	
	Top	11.46	9.371238	2.084952	
	Average	10.67	8.63	2.04	4.20

3.5.2 Ion Beam Milling Technique

Porosity values obtained using the ion beam milling technique were significantly lower than those obtained using the broken surfaces technique across the board with the exception of the sample taken at 12,555', which notably has the highest total organic carbon content of any sample. Values calculated for 3D porosity based upon 2D images are somewhat closer to those achieved by the broken surfaces technique; however, as the broken images technique provides a measurement of area porosity, and not volume porosity, the 2D porosity measurement would be a more appropriate comparison.

Table 7. Ion Beam Milling Porosity Values

Sample	3D Porosity	2D Porosity
12394	6.3	6.0
12469.5	5.3	3.4
12555	7.3	5.7
12593	4.5	2.3
12618	4.6	3.7

A possible explanation for these lower values could be due to the milling process. Much of the porosity detected in the broken surface technique is inorganic porosity, e.g. porous floccules and intraparticle pores; however, within the ion beam milled samples, there is essentially no inorganic porosity, with nearly all measured porosity being derived from organo-porosity (Slatt 2013). In plotting total organic carbon (TOC) against the porosity values derived from each technique, there is a trend

of lower TOC values being associated with more dissimilar, lower porosity values (Figures 39 and 40). Images used in each technique may be seen in figures 41 and 42.

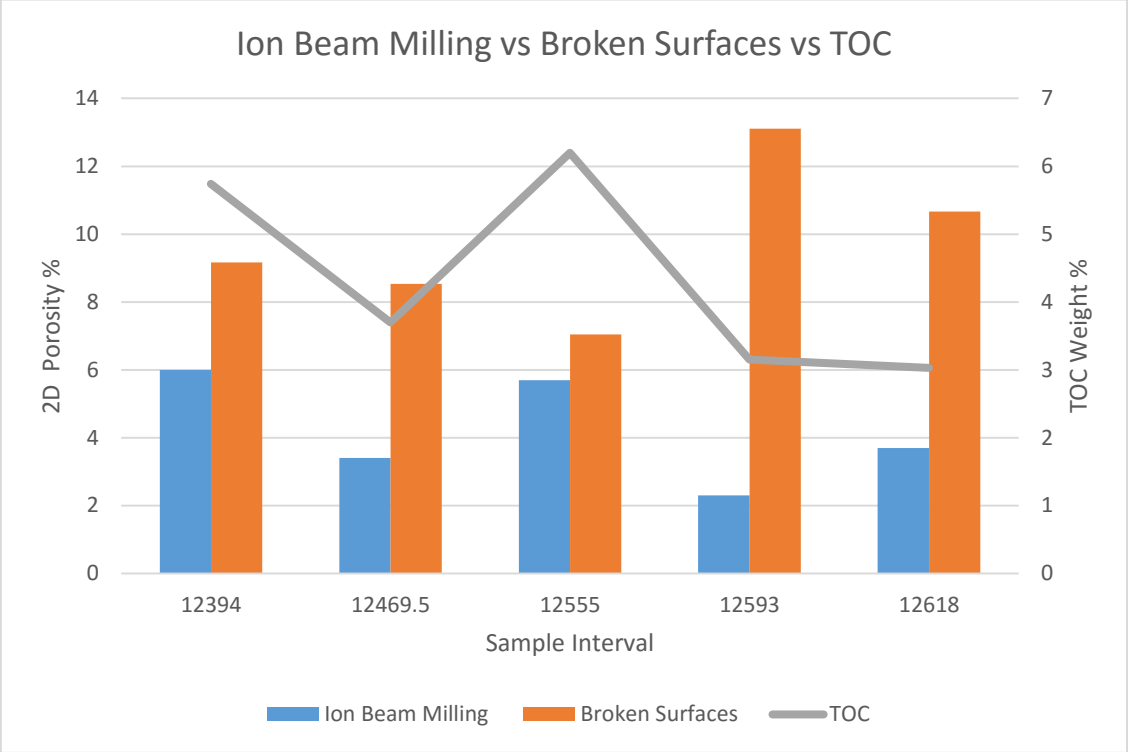

Figure 39. Comparison of porosity values derived from ion beam milling and the broken surfaces technique plotted against total organic content. Porosity values are universally higher in the broken surfaces technique likely due to the preservation of inorganic porosity. Additionally, porosity values are most similar in samples with high organic content and most dissimilar in samples with low organic content.

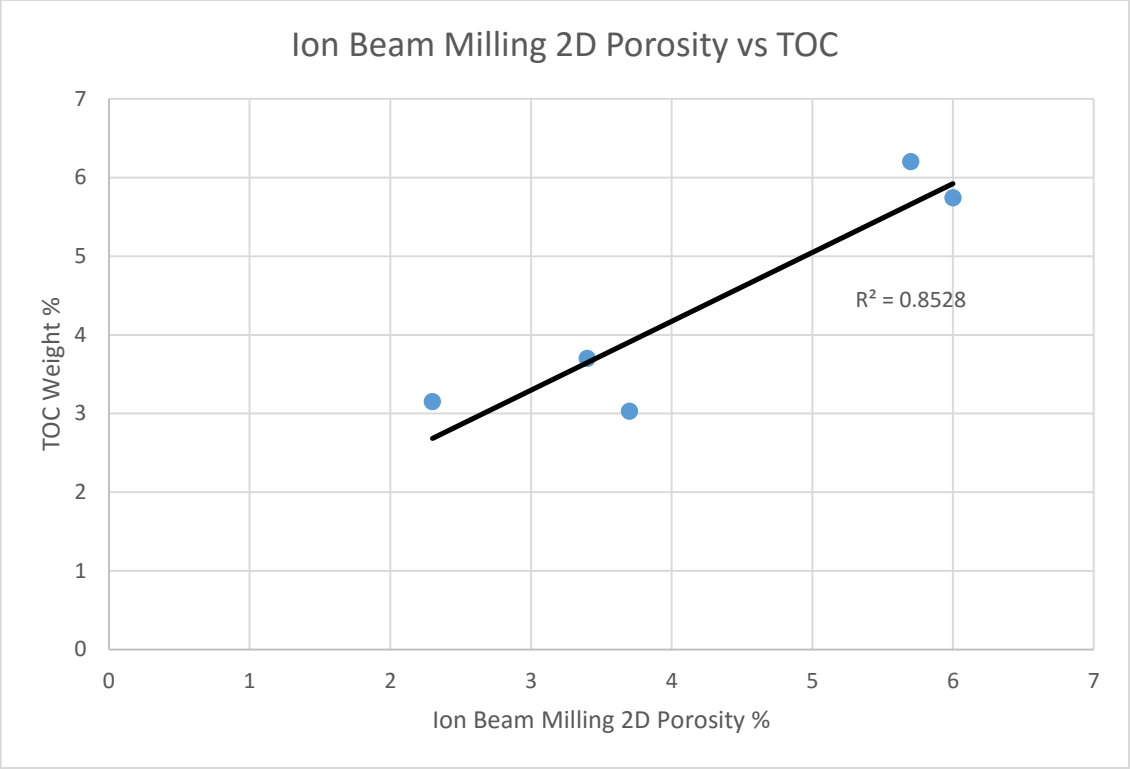

Figure 40. Graph showing relationship between total organic carbon and ion beam milling porosity values. The correlation reflects the tendency of ion beam milling to measure only organic porosity within the samples analyzed.

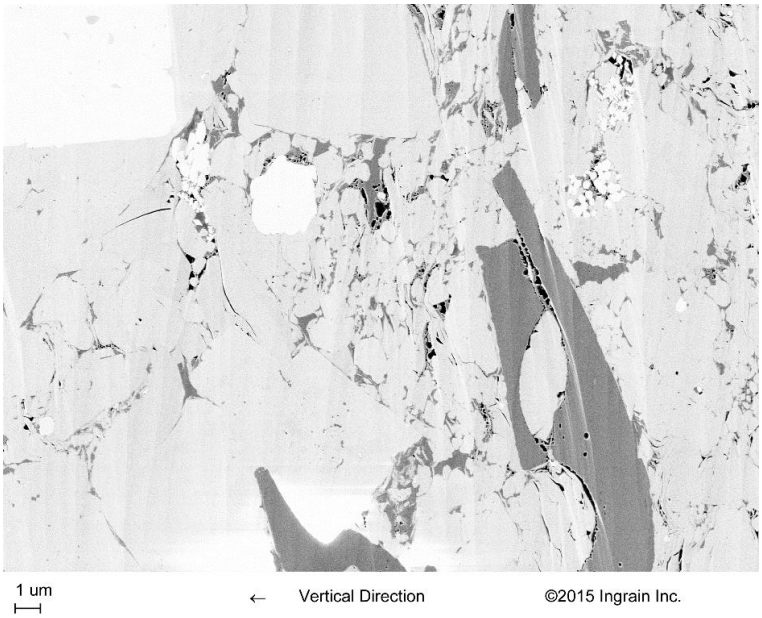

Figure 41. Ion beam milled sample used in porosity imaging. Taken from 12,593'. Porosity is highlighted in black. Note the general lack of pores present within the inorganic (light colored) material. This interval was determined to contain 2.3% 2D porosity using the ion beam milling technique.

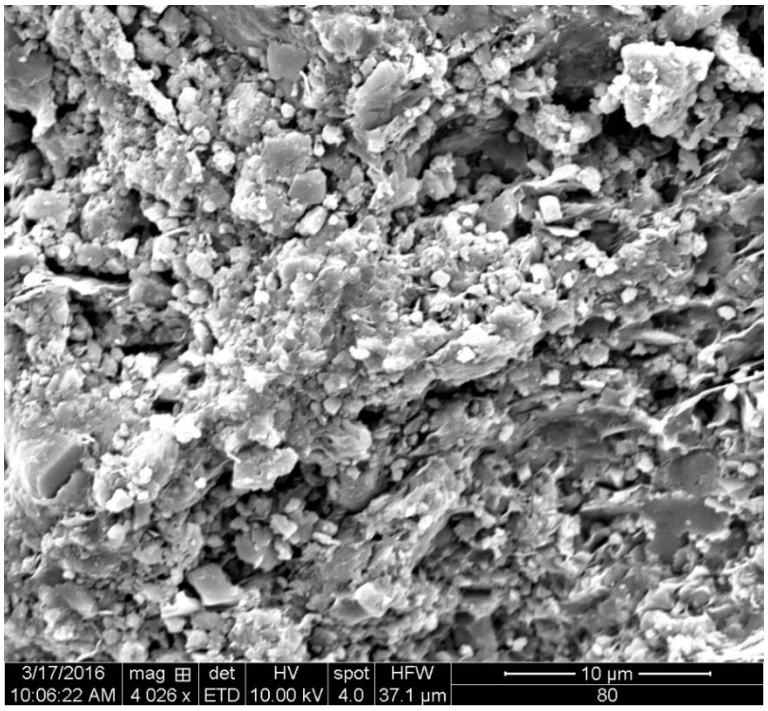

Figure 42. Broken surface sample used in porosity imaging. Taken from 12,593'. Porosity is highlighted in black. Note the presence of intergranular inorganic porosity. This interval was determined to contain 13.11% 2D porosity using the broken surfaces technique.

3.5.3 Calculated Density Technique

The third technique relied upon calculating the matrix density based upon X-ray diffraction mineralogy and RockEval organic content. The sample at 12,618’ had to be thrown out due to a large amount of amorphous silica within the sample, preventing accurate measurement of its mineralogy. Measurements produced values much greater than either of the other measurement technqiues. Values ranged from 14.46% to 31.5%, and are unrealistically high. The sole exception is the sample taken at 12593’, which was calculated to contain 16.7% porosity and is roughly comparable to the 13.11% measured via the broken surfaces technique. Although the measurement calculated for 12469.5’ is lower, both of the other techniques yielded much lower values for this sample at 5.3% for the ion beam milling technique and 8.53% for the broken surfaces technique. Given the unrealistically high values, this technique does not appear to be an accurate means of determining porosity.

Table 8. Calculated Density Porosity Values

DEPTH (ft)	MATRIX DENSITY	MEASURED VOLUME	MEASURED MASS	MEASURED DENSITY	POROSITY
12394.00	2.921564	7.30	16.26	2.23	23.75%
12555.00	2.968675	7.05	14.34	2.03	31.50%
12593.00	2.862023	8.55	20.38	2.38	16.71%
12469.50	2.87359	8.20	20.16	2.46	14.46%

4. DISCUSSION

4.1 SEQUENCE STRATIGRAPHY

Each of the two cores exhibit similar trends within a sequence stratigraphic framework, albeit with slightly different manifestations. These differences may be due to variations in the relative location of each core within their respective environments of deposition. In each core, units with an abundance of clay minerals represent a relatively low sea level, allowing for siliciclastic material to be deposited further from its source. In the chemostratigraphy, this is further evidenced by the close tracking of titanium and zirconium levels relative to aluminum, which serve as proxies of continental influx.

Focusing on the Boatwright, within the core description, there is far greater evidence of bioturbation and burrowing within the lower clay-rich interval of the core than anywhere else, further indicating a relatively shallow sea level in the environment of deposition, i.e. this unit represents the lowstand systems tract. Above the clay rich base is an apparent sequence boundary and maximum flooding surface, with a highly pyritized short interval containing an abundance of microfossils not seen in any other thin sections which could represent a condensed section (Figure 10-13). This is followed by a massive increase in the ratio of silicon to titanium and silicon to aluminum, indicative of a high degree of biogenic silica being produced, as well as a sharp decrease in the aluminum content (Figure 43). Combined, this indicates a rapid increase in sea level, as terrigenous siliciclastic input was deposited closer to the shore at that time, allowing for the production of biogenic silica in the deeper waters. This coincided with an increase in vanadium (V), molybdenum (Mo), and chromium (Cr) as well (Figure 29), all indicative of anoxic bottom water conditions, further evidencing a

deeper sea level at the time. Following the spike in silicon/titanium and silicon/aluminum ratios, the values for each remain consistently higher than those seen in the clay-rich base, although they exhibit a clear declining trend moving upward in the core as aluminum, titanium, and zircon increase, indicating a fall in sea level. Therefore, it is likely that the massive increase in silicon/aluminum and silicon/titanium ratios marks a maximum flooding surface, and the subsequent decrease in these ratios is representative of a falling stage systems tract.

In addition to the aforementioned sequence, there is evidence for a higher order sequence superimposed over it. Although it is expressed over the entirety of the core, this higher order sequence becomes most evident beginning at 12,973'. At this point, aluminum levels fall as silicon/aluminum and silicon/titanium levels again rise. This coincides with the largest concentration of vanadium in the core, further indicating sea level rise. At 12,964', aluminum levels begin to increase again, indicating a drop in sea level, whereupon at 12,960' this higher order cycle appears to complete, and sea level begins to rise again. There are two further higher order cycles present in the core, each measuring approximately 10 feet. (Figures 16 and 43)

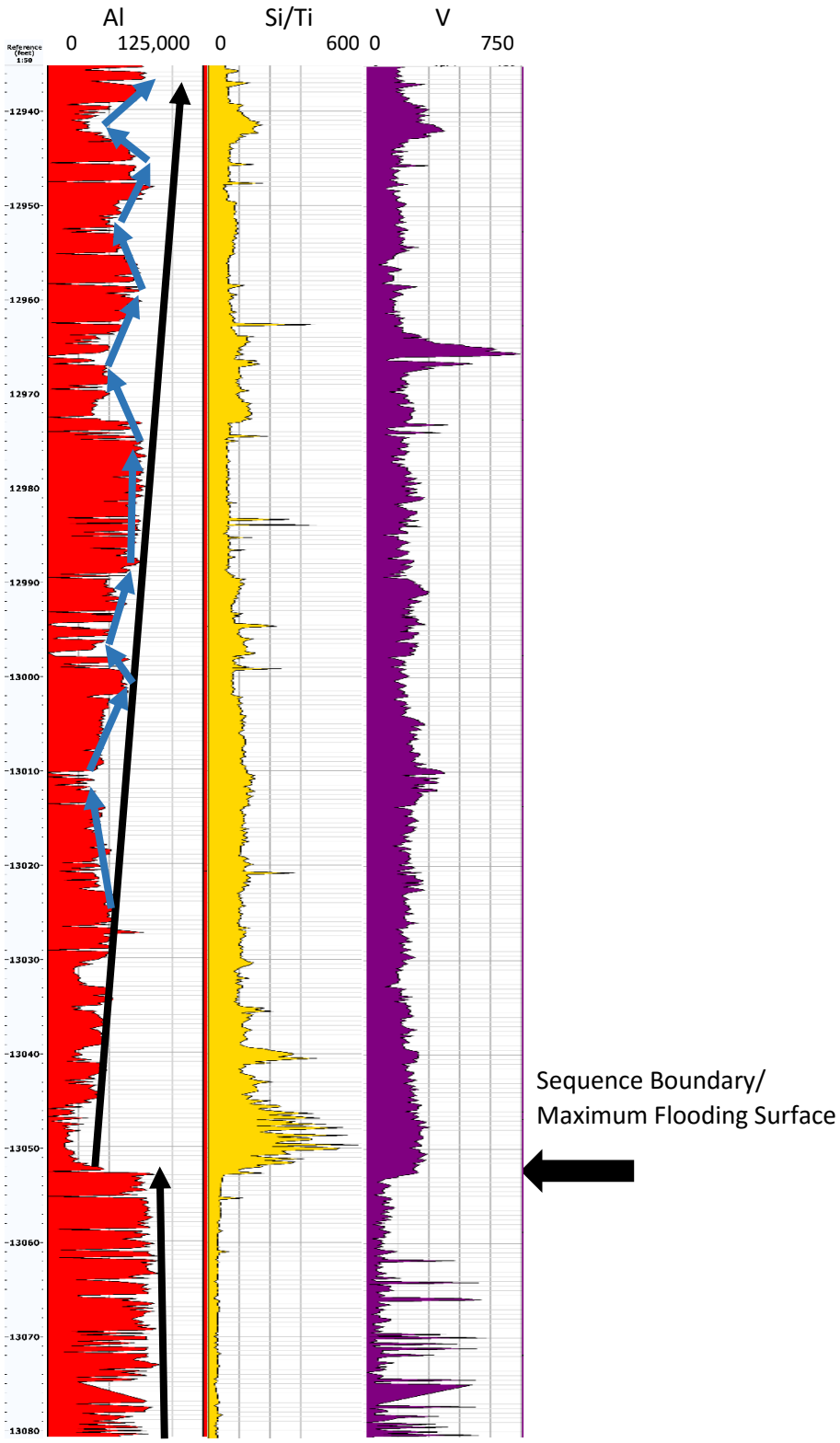

Figure 43. Aluminum, Silicon/titanium ratio, and Vanadium within Boatwright core. Lower order trends marked by black arrows on track, higher order by blue. Decreases in aluminum are mirrored by increases in silicon/titanium ratio and vanadium. All units in parts per million.

Shifting focus to the Velma core, the core begins much like the Boatwright with a clay-rich base, indicative of a lowstand systems tract. This clay-rich interval gradually decreases in clay content until 11,841' at which point the clay content drops sharply, being replaced by beds primarily composed of dolomite. (Figure 44) At this time, titanium and zirconium levels drop in kind, indicating a drop in terrigenous input and a rise in sea level. There are several other spikes in calcium and magnesium throughout the core, with a trend of increasing magnitude leading into it from the base and decreasing magnitude following it upsection. Following the primary dolomite bed, there is a gradual decrease in clay content, indicating another drop in sea level. Unlike the Boatwright core, the proxies for anoxia, namely molybdenum and chromium, markedly decrease in abundance in association with the rising water level at this point. Vanadium however was largely unchanged. Given the skeletal fragments and occasional coarse grained beds, it would appear that the dolomitic units are the result of a debris flow, similar to those seen in the Wolfcamp Shale (Wickard 2016) (Figure 45). The drop in anoxia proxies would be consistent with an influx of material from a shallow marine setting bringing oxygen into the environment of deposition. While debris flows are often associated with drops in sea level, rising sea levels could also lead to the accumulation of sediment along a shelf margin to the point at which it becomes unstable and collapses. Therefore, it is likely that the primary dolomite bed is indicative of the maximum flooding surface within the broad lower order cycle making up the core. This would reflect a similar trend in the Wolfcamp in which the debris flows are associated with highstand sea levels (Mazzullo 1997). There is no clear sequence boundary within this core section. The smaller calcium and magnesium rich units throughout the core

represent a higher order cycle superimposed onto the lower order cycle. Also of note is that silicon/aluminum and silicon/titanium ratios are consistently higher following the debris flow, indicative of a higher sea level retaining continental input near the shore, allowing increased biogenic silica production. Therefore, this section represents high stand systems tract, with the following decrease in silicon/aluminum and silicon/titanium ratios in the upper core representing a falling stage systems tract.

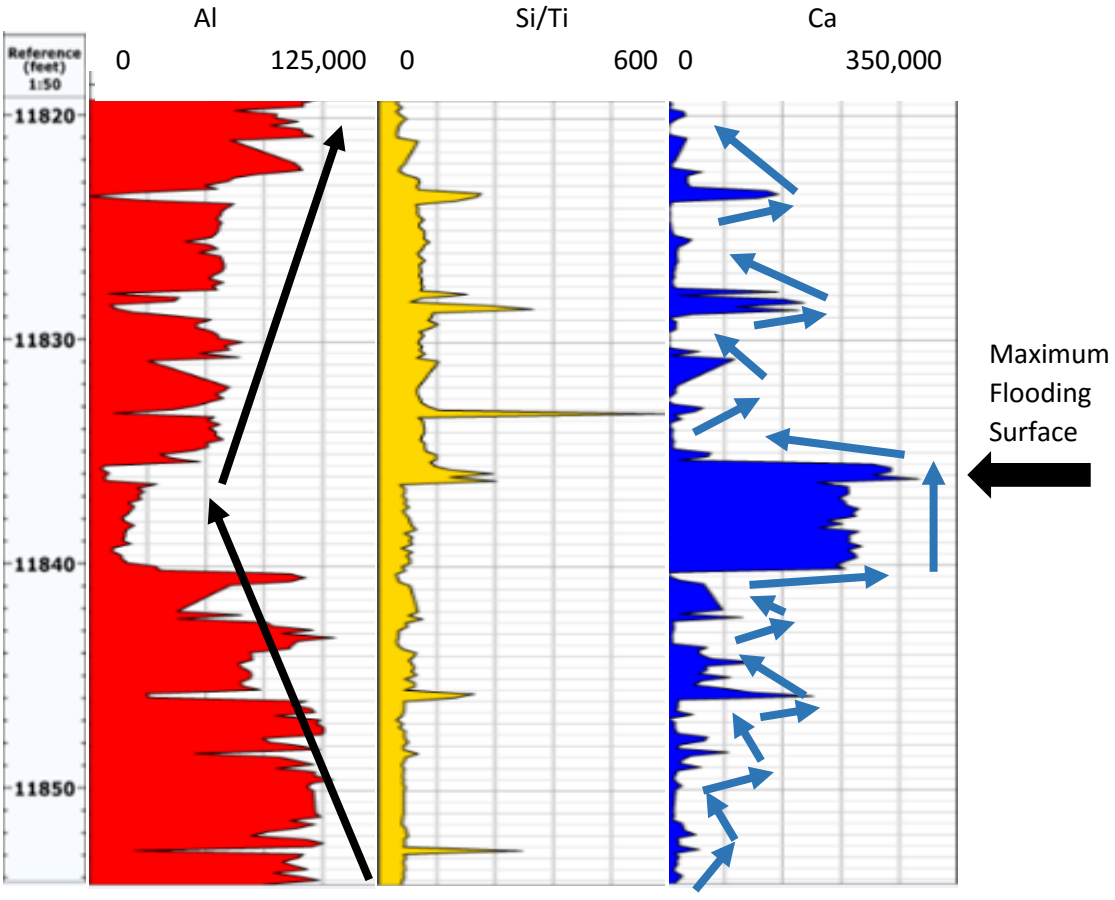

Figure 44. Aluminum, silicon/titanium ratio, and calcium within Velma core. Trend of the lower order cycle is indicated by the black arrows on the aluminum curve, while the higher order cycles are indicated by the blue arrows on the calcium curve. Decreases in aluminum content represent higher sea levels. Note the increase in the silicon/titanium ratio following the maximum flooding surface.

Figure 45. Dolomitic debris flow preserved in Velma core between 11,839' and 11,840'04". Note the coarse, reworked skeletal fragments between the 5" and 9" mark on the ruler outlined in red.

4.2 CONCLUSIONS

Being in the early stages of its development, there is a lot yet to be learned of the Goddard Shale. Given the limited scope of this study, there are still many questions to be answered. However, it is hoped that this study can begin to unravel the complexities of this formation.

Starting with that which is known, the Boatwright and Velma units within the Goddard Shale can be defined as siliceous-argillaceous shales with occasional influxes of carbonate debris flows from shallower water. In both cores there is an overall lower ordered cycle comprising each unit with a higher order cycle superimposed. The most brittle facies in the Velma are the dolomite beds, followed by the biogenic silica-rich intervals, and it stands to reason this would hold true for the Boatwright as well with the exception that there are intervals of the Boatwright which contain a greater quartz content than is present in the Velma. It is likely this facies would have a high hardness value, more similar to those observed in the dolomite-rich facies. While there are trends in the chemofacies in regards to the lithofacies, they do not directly correspond, and thus both must be taken into account in developing an interpretation of the formation. However, a strong trend does exist within the chemostratigraphy in that elevated thorium levels coincide with an elevated degree of continental input, allowing for targeting of more brittle zones through the use of a spectral gamma log.

The biggest question that remains somewhat unanswered is not unique to this formation, but is inherent to all unconventional resources: what is the porosity within the formation? Each of the techniques used produced very different results on adjacent samples, yet there is no true way to tell which of the results are correct. While this study

attempted a new technique derived from calculated density in the hopes that a third data point would align with either the ion beam technique or the broken surfaces technique, the results were unrealistic at best. In each of the techniques, there is room for a good deal of error to be introduced. In the calculated density method, there is a reliance upon accurate estimates of weight percentages based upon XRD. Furthermore, there is some variation in density, especially among clay minerals. Although a precise graduated cylinder was used, there is a margin of error inherent in water displacement measurements. While great care was taken to ensure that none of the sample was left behind when they were crushed for the degassing chamber, there were small amounts of dust that stuck to the equipment. Combined, these errors may account for the abnormally high measurements.

Shifting focus to the other techniques, using the broken surfaces SEM technique, a possible pitfall exists in that plucked grains may appear to be pore spaces. Although in most instances pores are easily differentiated from plucked grains, there is the chance to introduce error nonetheless. Using the ion beam technique, there is an apparent lack of inorganic porosity possibly due to the milling process which overlooks porosity that may exist within clay floccules or any sort of intergranular porosity. This inorganic porosity is important to the reservoir characterization as it would likely be more interconnected than porosity existing within isolated pockets of organic content (Murphy et al 2012, Slatt et al 2013). Additionally, as both of these techniques are reliant upon image analysis, another source of error may stem from the images themselves. As the analysis relies upon variations in light and dark to determine what is

pore space and what isn't, variations in the contrast and the brightness of the images can lead to drastically different results.

Finally, the issue inherent in all of these techniques is that of resolution. All of the techniques used are both time and resource intensive, meaning there are fewer data points that can reasonably be obtained than porosity measurements in conventional formations. The samples taken for porosity measurements cover an interval of 224 feet. Given the high level of heterogeneity present within unconventional resources, it seems unlikely that 5 samples could be fully representative of such a large interval. Furthermore, it can be difficult to determine if the measurements taken are even representative of the sample as a whole. The ion beam technique relies upon CT scans to determine what the most representative portion of the sample is, but even still, it relies upon a single data point in each sample. The broken surfaces technique attempts to overcome this by taking an average from several different points, but there is still the issue that the 5 samples taken are not representative of the formation as a whole. With all of that said, the broken surfaces technique appears to be the most accurate as it maintains the inorganic porosity of the sample while at the same time providing coverage of a larger area than the ion beam technique. Additionally, as the ion beam milling technique corresponds so closely to total organic content and provides increasingly disparate results compared to the broken surfaces technique in samples with a low organic content, it would appear that its measurements are more indicative of the organic content of the sample than the overall porosity within this formation.

Going forward on studying this formation, suggestions for future work would include regional mapping of the formation via well logs and seismic to determine its full

extent, and to determine the structural features present. Returning to the porosity issue, a more exhaustive porosity study could assist in finding finer scale porosity trends within the formation, as well as the specific types of porosity present. Additionally, based off of the correlation between total organic carbon and ion beam milling derived porosity with the available data, a study making use of a wider range of data sets from a number of different formations could establish a more firm relationship between the two. Finally, determining an outcrop location for the formation would greatly assist in any future endeavors to study this formation.

REFERENCES

Algeo, T. J., and H. Rowe, 2012, Paleoceanographic applications of trace-metal concentration data: Chemical Geology, v. 324, p. 6-18

Andrews, R. D., 2001, Springer Gas Play in Western Oklahoma: Oklahoma Geological Survey Special Publication, 130 p.

Blakey, R. C., 2013, Late Mississippian North American Paleogeographic Map: < https://www2.nau.edu/rcb7/namM325.jpg> Accessed June 22, 2016.

Brumsack, H. J., 2006, The trace metal content of recent organic carbon-rich sediments: Implications for Cretaceous black shale formation: Paleogeography, Palaeoclimatology, Palaeoecology, v. 232, p. 344-361

Davis, C. Y., W. L. Manger, S. E. Lemke, 2015, Reservoir Characteristics of the Springer Shale in the SCOOP Play of the Eastern Anadarko Basin, Oklahoma: Ardmore Geological Society Meeting

Harris, N. B., C. A. Mnich, D. Selby, and D. Korn, 2013, Minor and trace element and Re-Os chemistry of the Upper Devonian Woodford Shale, Permian Basin, west Texas: Insights into metal abundance and basin processes: Chemical Geology, v. 356, p. 76-93

Mazzulo, S. J., 1997, Stratigraphic exploration plays in Ordovician to Lower Permian strata in the Midland Basin and on the Eastern Shelf: Publications- West Texas Geological Society, p. 1-38

Murphy, M., J. Daniels, D. Cole, J. Sheets, and S. Welch, 2012, Pore distribution in the Ordovician Shale of the Utica/Point Pleasant sub-basin: AAPG Search and Discovery Article #50605, AAPG Annual Convention and Exhibition, Long Beach, Calif. 2012.

Nash, S. S., 2014, The Springer Shale: A Sleeping Giant?: AAPG Search and Discovery Article #10664

Peace, H. W. II, 1965, The Springer Group of the Southeastern Anadarko Basin in Oklahoma: The Shale Shaker Digest V, Volumes XV-XVII (1964-1967), p. 280-297

Reedy, H. J., 1968, Carter-Knox Gas Field, Oklahoma: Natural Gases of North America, v. 2, p. 1476-1491

Sageman, B. B., and T. W. Lyons, 2004, Geochemistry of fine-grained sediments and sedimentary rocks: Treatise on geochemistry, v. 7, p. 115-158

Slatt, R. M., N. O'Brien, C. Molinares-Blanco, A. Serna-Bernal, E. Torres, P. Philp, 2013, Pores, Spores, Pollen and Pellets: Small, but Significant Constituents of Resource Shales, Unconventional Resources Technology Conference, p. 17

Smith, P. W., W. J. Hendrickson, C. M. Williams, 1996, Regional Correlations and Reservoir Characterization Studies of the Springer Group in the Anadarko Basin Area of Western Oklahoma: Transactions of the 1995 AAPG Mid-Continent Section Meeting, p. 116-126

Treaton, J. A., 2014, Outcrop derived chemostratigraphy of the Woodford Shale, Murray County, Oklahoma: M.S. thesis, University of Oklahoma, Norman, OK, 100 p.

Tribovillard, N., T. J. Algeo, T. Lyons, and A. Riboulleau, 2006, Trace metals as paleoredox and paleoproductivity proxies: An update: Chemical Geology, v. 232, p. 12-32

Westheimer, J. M., 1956, The Goddard Formation: Petroleum Geology of Southern Oklahoma, v. 1, p. 392-396

Wickard, A. K., 2016 A Diagenetic Study of the Wolfcamp Shale in the Midland Basin, West Texas: M.S. thesis, University of Oklahoma, Norman, OK, 83 p.